

A Two-Stage Bayesian Framework for Multi-Fidelity Online Updating of Spatial Fragility Fields

Abdullah M. Braik^a and Maria Koliou^{b*}

^{a)} Postdoctoral Research Associate, Zachry Department of Civil and Environmental Engineering, Texas A&M University, College Station, TX, 77843, U.S.A., E-mail: abraik3@tamu.edu

^{b)} Associate Professor and Zachry Career Development Professor II, Zachry Department of Civil and Environmental Engineering, Texas A&M University, College Station, TX, 77843, U.S.A., E-mail: maria.koliou@tamu.edu (*Corresponding author)

A Two-Stage Bayesian Framework for Multi-Fidelity Online Updating of Spatial Fragility Fields

Abstract

This paper addresses a long-standing gap in natural hazard modeling by unifying physics-based fragility functions with real-time post-disaster observations. It introduces a Bayesian framework that continuously refines regional vulnerability estimates as new data emerges. The framework reformulates physics-informed fragility estimates into a Probit-Normal (PN) representation that captures aleatory variability and epistemic uncertainty in an analytically tractable form. Stage 1 performs local Bayesian updating by moment-matching PN marginals to Beta surrogates that preserve their probability shapes, enabling conjugate Beta-Bernoulli updates with soft, multi-fidelity observations. Fidelity weights encode source reliability, and the resulting Beta posteriors are re-projected into PN form, producing heteroscedastic fragility estimates whose variances reflect data quality and coverage. Stage 2 assimilates these heteroscedastic observations within a probit-warped Gaussian Process (GP), which propagates information from high-fidelity sites to low-fidelity and unobserved regions through a composite kernel that links space, archetypes, and correlated damage states. The framework is applied to the 2011 Joplin tornado, where wind-field priors and computer-vision damage assessments are fused under varying assumptions about tornado width, sampling strategy, and observation completeness. Results show that the method corrects biased priors, propagates information spatially, and produces uncertainty-aware exceedance probabilities that support real-time situational awareness.

Keywords:

Spatial Fragility Modeling; Bayesian Updating; Multi-Fidelity Data Integration; Online Learning; Heteroscedastic Gaussian Processes; Tornado Damage Assessment; Digital Twin.

1. Introduction

1.1. *Motivation and Problem Setting*

Natural hazards continue to challenge communities worldwide, revealing persistent gaps in our ability to anticipate, characterize, and interpret structural damage. Despite advances in engineering design, hazard modeling, and resilience planning, the observed performance of the built environment under extreme loading frequently diverges from model predictions. These discrepancies stem from substantial aleatory uncertainties in hazard intensity and structural capacity, as well as epistemic uncertainties embedded in the assumptions used to represent them.

Before hazard, risk assessments rely on probabilistic vulnerability models derived from physics-based simulations, empirical data from past events, heuristic rules, or hybrid formulations. These models are indispensable for mitigation and preparedness planning, yet their usefulness is largely confined to the pre-event phase. Once a hazard unfolds, fragility-based predictions remain static and cannot adapt to evolving conditions or observed building performance, causing prediction accuracy to degrade when real conditions diverge from idealized assumptions.

After a hazard, actual damage has occurred, and low-fidelity pre-event predictions quickly become insufficient once observational data begins to emerge. Field inspections, post-disaster imagery, aerial surveys, and crowdsourced reports provide direct evidence of building performance across affected regions. However, these data streams are often incomplete, delayed, and heterogeneous in fidelity. More critically, they rarely enter a statistically principled framework capable of assimilating them and updating prior predictions.

As a result, pre-event vulnerability models and post-event observations have progressed along parallel tracks, even though the limitations of one align almost perfectly with the strengths of the other. Without a unified framework to connect them, vulnerability models remain disconnected

from the evidence that could refine them, while observational data lacks a coherent prior for rigorous inference. This disconnect represents a missed opportunity to develop dynamic digital twins that operate before and after a hazard, adapt to varying data fidelity and coverage, and provide a principled mathematical foundation for real-time decision support.

1.2. Background on The Development of Fragility Models Within Probabilistic Risk Assessment

Fragility modeling emerged from the evolution of structural reliability theory, which reframed structural safety as a probabilistic event influenced by uncertainty in both loading and resistance. Early foundational work introduced limit-state formulations, reliability indices, and probability-of-failure concepts, enabling structural performance to be quantified probabilistically rather than through fixed safety factors [1-3]. These ideas permeated modern design practice through load- and resistance-factor methodologies [4], shifting vulnerability assessment away from deterministic margins toward explicit representations of uncertainty. Within this context, fragility functions emerged as practical tools for expressing the probability that hazard demand exceeds structural capacity [5], accelerating adoption during the rise of performance-based earthquake engineering. Early seismic applications, commonly modeled using lognormal exceedance curves, supported scalable regional loss estimation [6, 7] and informed methodologies that remain central to contemporary practice [8].

Over the past two decades, fragility modeling has expanded across hazards, building types, and infrastructure systems [9]. In earthquake engineering, empirical, experimental, and simulation-based methods have produced multi-state fragilities for reinforced concrete systems [10-13], steel systems [14-16], wood systems [17, 18], and nonstructural components [19]. Incremental dynamic

analysis [20] further strengthened the statistical treatment of record-to-record variability and improved the robustness of fragility modeling.

Fragility concepts were subsequently extended to other hazards. For hurricanes, fragility functions have been developed for wind effects on low-rise residential structures [21-23], flood impacts [24-26], and storm-surge or wave-induced damage [27, 28]. Tornado-specific fragilities have been generated for buildings subjected to highly localized extreme wind fields [29-31]. Beyond buildings, fragility modeling has informed risk assessments for bridges [32-34], electric power networks [35-38], and pipeline systems [39, 40].

Today, fragility functions support a wide range of applications, including regional loss estimation [41], performance-based engineering [42], and mitigation planning at the community scale [43]. Yet even the most advanced fragility models remain fundamentally pre-event constructs. Their mathematically structured form positions them naturally as priors for post-event inference, but this capability remains largely unrealized. Progress in this direction requires frameworks that treat fragility functions as updatable Bayesian priors, capable of continuous refinement as heterogeneous, multi-fidelity observations become available after a hazard.

1.3. Background on Post-Disaster Data and Damage Assessment

Rapid and reliable post-disaster damage assessment is essential for emergency response, loss estimation, and early recovery planning. Traditional assessment relied on ground surveys, windshield inspections, and reconnaissance teams, which delivered detailed building-level information but required substantial time, labor, and physical access to affected areas [44, 45]. While important for long-term model refinement and code calibration [46-48], these methods remain insufficient for real-time decision-making immediately after a hazard.

Remote sensing has expanded the achievable scale and timeliness of post-disaster assessments. Unmanned Aerial Vehicle (UAV) imagery offers fine spatial resolution for detailed structural evaluation, whereas aerial and satellite imagery provide rapid, large-area coverage essential for regional situational awareness [49]. In parallel, deep learning has become the dominant approach for automating damage inference from these imagery sources [50-53].

Beyond computer vision, other post-disaster data streams have emerged. Social sensing and outage reports offer indirect indicators of damage [54, 55], while crowdsourcing platforms provide rapid, human-generated observations at scale [56]. Although these sources broaden the available evidence, they also amplify challenges of heterogeneity, partial coverage, and variable fidelity.

Despite these advances, most post-disaster approaches remain fundamentally data-driven and lack grounding in physics-based vulnerability principles or statistically coherent inference. Some recent studies attempt to model uncertainty, such as uncertainty-aware crowdsourcing frameworks [57] and uncertainty-aware deep learning models for aerial-image classification [58], but these methods quantify uncertainty within their respective data sources rather than linking observations to prior structural vulnerability or enabling principled Bayesian updating. They do not reconcile inconsistent evidence, propagate information into unobserved areas, or integrate multi-fidelity observations within a unified probabilistic framework. In practice, data arrives gradually, with inconsistent fidelity and substantial spatial gaps. These limitations underscore the need for methodologies that incrementally update pre-event priors, assimilate heterogeneous post-disaster observations, and quantify uncertainty in a coherent statistical structure.

1.4. Background on Efforts to Integrate Predictive Risk Assessment with Adaptive Data

Assimilation and the Resulting Research Gap

Recent efforts have attempted to bridge pre-event predictive modeling with post-disaster data assimilation, but existing approaches remain fragmented and limited in scope. Some work has focused on adaptive data collection, such as the strategy introduced by Behrooz, Ilbeigi [59], which employs an ordinal gradient-boosting model and a multi-objective sampling scheme to prioritize informative buildings. However, these approaches rely on heuristic pre-event predictors and lack statistically coherent update mechanisms anchored in prior vulnerability functions. Other advances explore reinforcement learning to guide autonomous robotics for reconnaissance and search-and-rescue [60], though these efforts emphasize operational efficiency rather than principled updating of structural performance predictions.

Complementary research has incorporated post-disaster observations into broader risk and recovery frameworks. For example, Braik and Koliou [61] combined remote sensing, GIS, and deep learning to automate post-event damage assessment and used the resulting outputs for recovery forecasting. Building on this, Braik, Han [62] used computer-vision-derived damage states to initialize agent-based recovery models and to back-infer tornado wind fields. While valuable, these approaches assume timely, high-fidelity, and spatially complete observations—conditions rarely met immediately after a disaster—and do not provide a unified statistical foundation for dynamically updating fragility-based predictions.

Despite these advances, no existing method enables a principled Bayesian integration of pre-event fragility priors with incrementally arriving, heterogeneous post-disaster data, nor do current tools accommodate multi-fidelity observations or quantify layered aleatory and epistemic uncertainties during the updating process. While hierarchical Bayesian formulations have been

explored [63, 64], these efforts have largely focused on parameter estimation and have not addressed real-time updating, spatial propagation of uncertainty, or fusion of mixed-quality evidence.

A second major gap concerns the global propagation of local information. For interconnected systems such as electric power networks, Bayesian network–based digital twins have demonstrated how knowledge acquired at one component can inform others through principled dependency structures [65, 66]. However, structural building damage is inherently spatial rather than network-based, requiring models that encode proximity, correlation decay, and cross-archetype relationships. Recently, Braik and Koliou [67] proposed a spatial fragility modeling framework based on a warped Gaussian Process (GP) that represents fragility as a coherent field across space, archetypes, and damage states. While this approach establishes a strong mathematical foundation for spatial inference, its deployment for sequential updating and online data assimilation remains underexplored.

Collectively, these limitations reveal a critical research gap: there is no unified, mathematically coherent, dynamically updatable digital-twin framework that links pre-event fragility models with evolving post-disaster observations, propagates information spatially, and accommodates incomplete, heterogeneous, multi-fidelity data. Developing such a framework is essential for maintaining robust risk assessments before, during, and after a hazard event.

2. Methodology

The proposed methodology develops an online Bayesian learning framework for fragility modeling that continually refines physics-based predictions as new observations become available. It combines two complementary stages: a local updating stage that assimilates heterogeneous evidence to correct physics-based fragility estimates, and a global propagation stage that uses a

structured GP to generalize these corrections across space and archetypes. This produces a coherent, end-to-end spatial learning pipeline that updates fragility estimates where direct evidence is available and transfers information to unobserved locations via kernel learning and hyperparameter tuning.

The framework begins by redefining conventional physics-based fragility functions as low-fidelity Probit–Normal (PN) priors. This anchors the learning process in established physics and keeps inference physically consistent even when data are sparse. The PN form captures both aleatory variability and epistemic uncertainty in an analytically tractable latent fragility index, providing a coherent baseline from which data-driven updates can evolve. In this way, the model first learns from physics and then from data, preserving interpretability and stability during early information scarcity.

The **first Bayesian stage** performs local updating of these PN priors. Each PN marginal is moment-matched to a Beta surrogate, enabling conjugate inference without the need for Markov chain Monte Carlo (MCMC) simulation. This mapping preserves the mean and variance of the PN distribution while maintaining statistical fidelity to its shape. Heterogeneous data sources are then assimilated through soft exceedance probabilities, with reliability weights encoding epistemic confidence. The resulting Beta posteriors are projected back into PN form, producing fragility observations whose variances reflect data fidelity—large for prior-only or uncertain sites and small where high-quality evidence is available. In this way, the model evolves from physics-based pseudo-observations toward increasingly data-driven fragility estimates as information accumulates.

The **second Bayesian stage** enables global learning and spatial generalization. It employs a GP defined over the latent fragility index, where each updated PN parameter serves as a pseudo-

observation that informs spatially and structurally similar points. The GP acts as a probabilistic interpolator across space and archetype, allowing information from data-rich or high-confidence sites to diffuse into unobserved or high-uncertainty regions. Working in the probit-transformed Gaussian domain preserves analytical tractability and yields closed-form means, variances, and correlations of exceedance probabilities. The result is a spatially coherent, physically informed, and uncertainty-aware fragility field that connects local evidence to regional understanding.

Together, these two Bayesian stages form a self-correcting probabilistic system: the local conjugate updates maintain consistency with incoming data, while the GP propagation enforces spatial and structural coherence across the inventory. This transforms fragility modeling from static prediction to a dynamic probabilistic field that continually learns and adapts as new evidence becomes available.

The overall workflow is summarized in Figure 1, with details provided in §2.1–2.3.

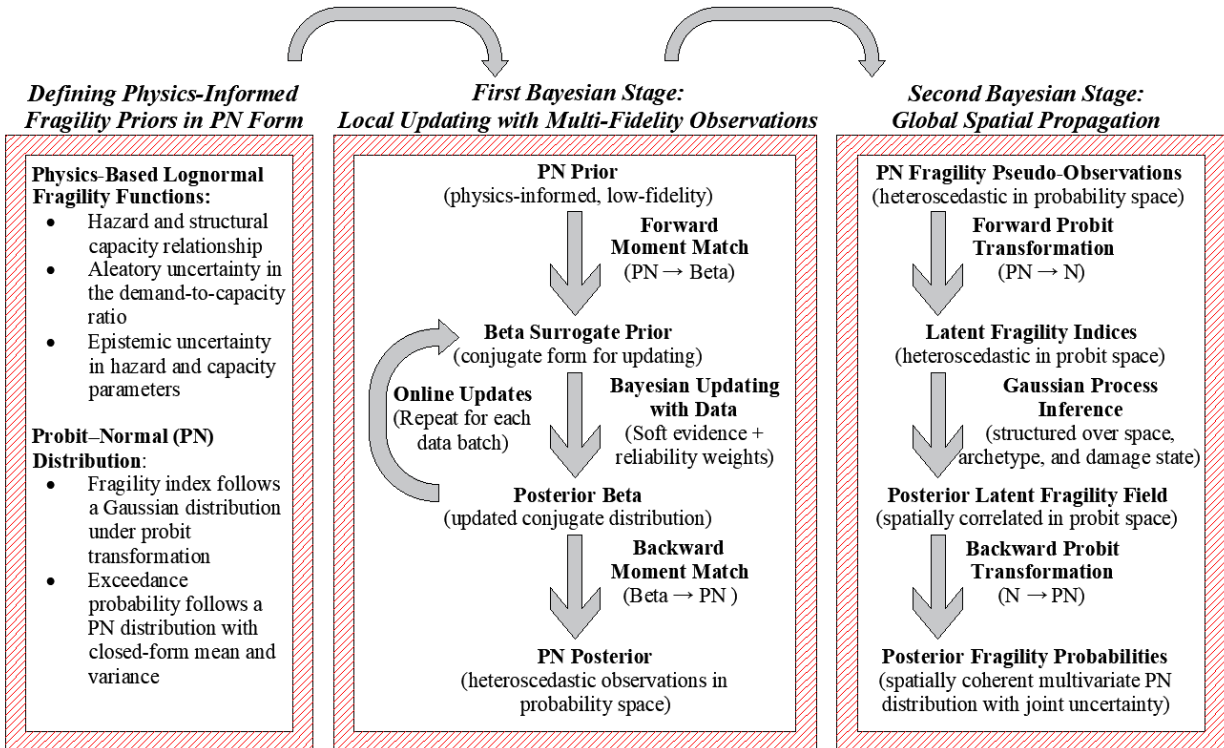


Figure 1: Flowchart of the Proposed Two-Stage Bayesian Fragility Modeling Framework

2.1. Defining Physics-Informed Fragility Priors in Probit-Normal Form

In the present framework, physics-based fragility functions are employed as low-fidelity prior of exceedance probabilities. Let n_s denote the number of buildings in the inventory and n_d the number of ordinal damage states. For each building at a geographic location s_i with $i \in \{1, \dots, n_s\}$ and damage state d_j with $j \in \{1, \dots, n_d\}$, the probability of exceeding d_j is expressed as:

$$P_{ij} := \Pr(D_i \geq d_j) = \Phi\left(\left(\ln(H_i) - \ln(C_{ij})\right) / \beta_{ij}\right) \in (0,1) \quad (1)$$

where $\Phi(\cdot)$ denote the standard normal cumulative distribution function (CDF), H_i is a random variable representing the hazard intensity at the location s_i , C_{ij} is a random variable representing the median capacity threshold corresponding to the damage state d_j for building i , and β_{ij} is the logarithmic standard deviation (dispersion) of the fragility function for damage state d_j of building i , reflecting aleatory variability in the demand-to-capacity ratio;

Equation (1) represents the standard lognormal fragility formulation commonly used in both seismic and wind engineering applications. To extend this formulation into a low-fidelity physics-informed prior, epistemic uncertainties in the hazard and capacity terms are included. These uncertainties are treated as lognormal random variables:

$$\begin{aligned} \ln(H_i) &\sim \mathcal{N}(\lambda_{H,i}, \beta_{H,i}^2) \\ \ln(C_{ij}) &\sim \mathcal{N}(\lambda_{C,ij}, \beta_{C,ij}^2) \end{aligned} \quad (2)$$

where $\lambda_{H,i}, \beta_{H,i}$ denote the mean and standard deviation of $\ln(H_i)$, while $\lambda_{C,ij}, \beta_{C,ij}$ denote the mean and standard deviation of $\ln(C_{ij})$. Hence, $\beta_{H,i}$ and $\beta_{C,ij}$ capture epistemic uncertainties associated with hazard estimation and damage state threshold, respectively.

A latent fragility index is defined by applying the probit transform to the exceedance probability:

$$Z_{ij} := \Phi^{-1}(P_{ij}) = \left(\ln(H_i) - \ln(C_{ij}) \right) / \beta_{ij} \quad (3)$$

Given the assumptions above, the latent variable follows a normal distribution:

$$Z_{ij} \sim \mathcal{N}(\mu_{ij}, \sigma_{ij}^2) \quad (4)$$

with mean and variance

$$\begin{aligned} \mu_{ij} &= (\lambda_{H,i} - \lambda_{C,ij}) / \beta_{ij} \\ \sigma_{ij}^2 &= (\beta_{H,i}^2 + \beta_{C,ij}^2) / \beta_{ij}^2 \end{aligned} \quad (5)$$

Thus, the exceedance probability becomes a bounded random variable through the probit transformation of the Gaussian latent index:

$$P_{ij} = \Phi(Z_{ij}) \sim \mathcal{PN}(\mu_{ij}, \sigma_{ij}^2) \in (0,1) \quad (6)$$

The resulting exceedance probabilities $\{P_{ij}\}$ therefore follow a Probit–Normal (PN) distribution, for which closed-form expressions for the mean and variance are available [67]:

$$\begin{aligned} m_{ij} &:= E[P_{ij}] = \Phi(\nu_{ij}) \\ \zeta_{ij} &:= \text{Var}[P_{ij}] = \Phi_2(\nu_{ij}, \nu_{ij}, \eta_{ij}) - \Phi(\nu_{ij})^2 \end{aligned} \quad (7)$$

where:

$$\begin{aligned} \nu_{ij} &:= \mu_{ij} / \sqrt{1 + \sigma_{ij}^2} \\ \eta_{ij} &:= \sigma_{ij}^2 / (1 + \sigma_{ij}^2) \end{aligned} \quad (8)$$

2.2. First Bayesian Stage: Local Updating with Multi-Fidelity Observations

2.2.1. Moment Matching Between Probit–Normal and Beta Distributions

While the PN distribution provides the canonical representation of exceedance probabilities derived from physics-based fragility (§2.1), it lacks the conjugacy required for efficient Bayesian updating with Bernoulli-type observations. By contrast, the Beta distribution is the natural conjugate prior for binomial and Bernoulli likelihoods [68], and therefore serves as an ideal vehicle

for analytic data assimilation. To bridge these two representations, a moment-matched Beta surrogate is introduced.

A Beta distribution $\mathcal{B}(\alpha_{ij}, \gamma_{ij})$ is defined by equating its first two moments to (m_{ij}, ζ_{ij}) of the PN distribution defined earlier in §2.1:

$$\begin{aligned}\alpha_{ij} &= m_{ij}\varpi_{ij} \\ \gamma_{ij} &= (1 - m_{ij})\varpi_{ij}\end{aligned}\quad (9)$$

where:

$$\varpi_{ij} = m_{ij}(1 - m_{ij})/\zeta_{ij} - 1 \quad (10)$$

The feasibility is guaranteed by the inequality $0 < \zeta_{ij} < m_{ij}(1 - m_{ij})$, which is always satisfied for PN marginals.

This construction is more than heuristic. The Beta surrogate preserves the exact mean and variance of the PN distribution while simultaneously enabling analytic conjugacy. Beyond the moment match, the two distributions are very similar in shape. Figure 2 compares PN and Beta densities across representative μ and σ^2 values. The match is nearly indistinguishable across the operational domain of interest, with discrepancies appearing only in the extreme tails, where probabilities approach 0 or 1.

The information loss incurred by substituting PN with its moment-matched Beta surrogate is quantified using the Kullback–Leibler divergence (D_{KL}) [69]. Figure 3 shows heatmaps of $D_{KL}(\text{PN}||\text{Beta})$ and $D_{KL}(\text{Beta}||\text{PN})$ over $\mu \in [-3, 3]$ and $\sigma^2 \leq 3$. Two insights emerge. First, across the entire range, D_{KL} remains below 0.11, which corresponds to less than 0.11 bits of expected excess information loss per update, which is considered negligible in the information-theoretic interpretation of D_{KL} [69, 70]. Second, the regions of nonzero D_{KL} correspond to cases where $|\mu|$ is large, and σ^2 is small, i.e., where the fragility distribution is nearly deterministic with

probabilities pinned near 0 or 1. In these regimes, the posterior updates are effectively deterministic because both PN and Beta yield near-zero variance, and hence, the exact shape of the PDF is of little engineering consequence. In the transition regions, where uncertainty is greatest and engineering decisions are most sensitive, D_{KL} is almost zero, indicating that the Beta surrogate is an almost exact proxy for PN.

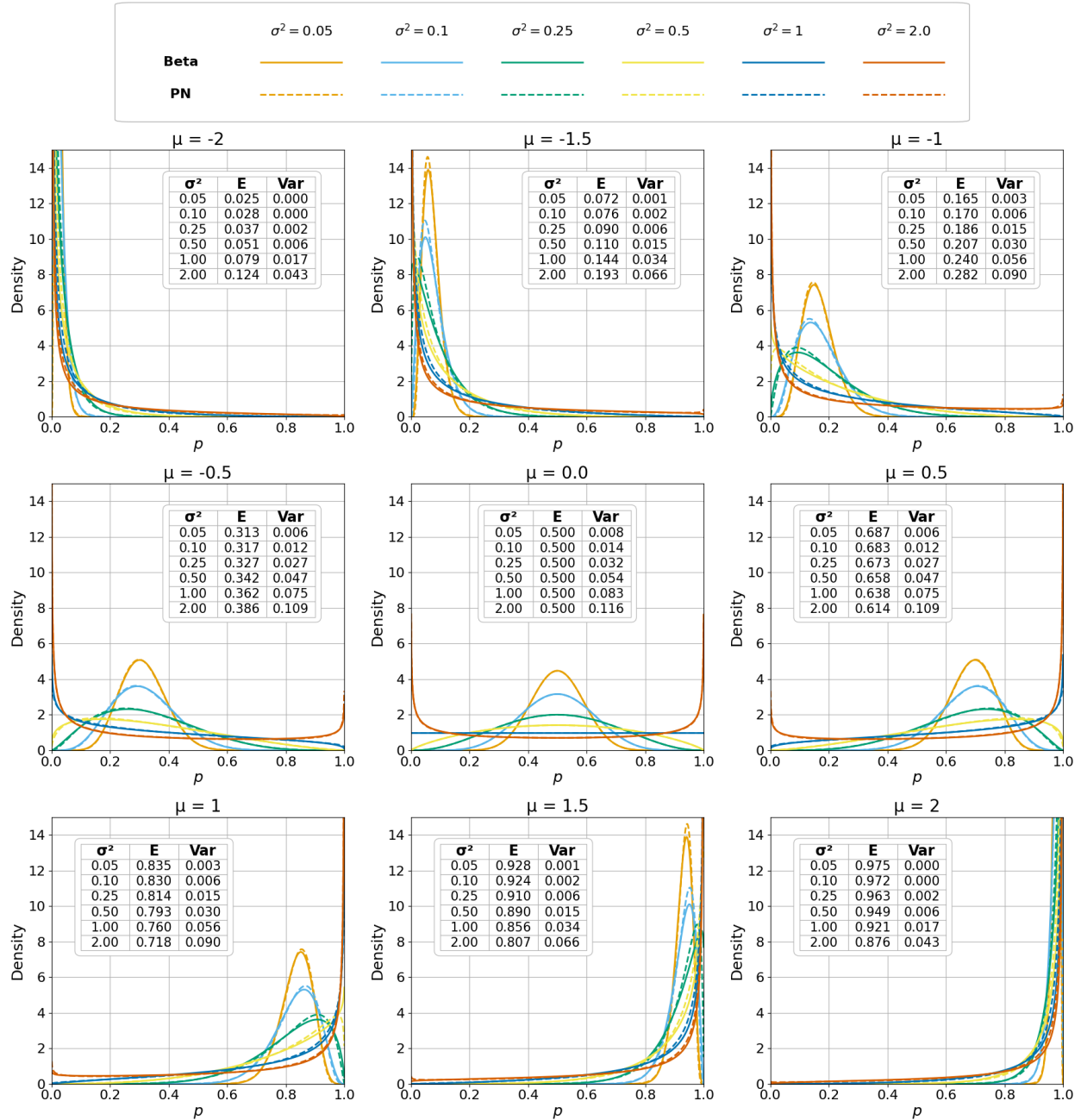


Figure 2: Comparison of PN and Beta Distributions Across Representative Parameters

Accordingly, the moment-matched Beta distribution provides a principled and empirically validated surrogate for PN marginals: it retains exact moment information, incurs negligible information loss, and enables conjugate Bayesian updating. Within the framework, the PN distribution remains the canonical representation for spatial Gaussian process modeling (§2.3), while the PN–Beta–PN pipeline serves as the computational mechanism for efficient online data assimilation (§2.2.2).

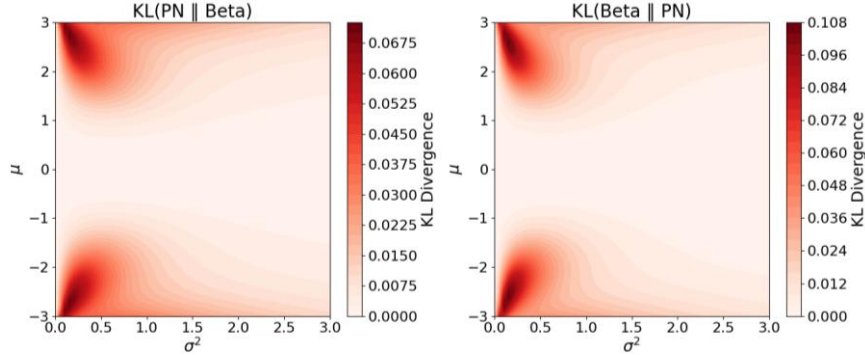


Figure 3: KL Divergence Between PN and Beta Distributions Over Parameter Space

2.2.2. Bayesian Updating with Multi-Fidelity Observations

The moment-matched Beta surrogate introduced in §2.2.1 enables closed-form Bayesian updating when new evidence becomes available. In practice, observations may be derived from diverse sources such as satellite and aerial imagery processed by machine learning classifiers [53], rapid visual inspections [71], or sensor-based measurements [72]. These sources vary in reliability and resolution and introduce two distinct forms of uncertainty. The first is aleatory variability, which is captured by the probabilistic outputs of the data source. The second is epistemic uncertainty, which reflects the trustworthiness of the source and is encoded as a weight factor calibrated using independent validation data.

For building i and damage exceedance threshold d_j , source b provides a probabilistic statement of exceedance denoted by $y_{ij}^{(b)} \in (0,1)$. This represents the aleatory uncertainty in whether $D_i \geq$

d_j . In cases where the source outputs categorical probabilities $\{\mathfrak{J}_{i\chi}^{(b)}\}_{\chi=1}^{n_d}$ for individual damage states, the exceedance probability is obtained by cumulative aggregation:

$$y_{ij}^{(b)} = \sum_{\chi \geq j} \mathfrak{J}_{i\chi}^{(b)} \quad (11)$$

Thus, $y_{ij}^{(b)}$ constitutes a soft observation of the exceedance event, directly encoding the variability conveyed by the source, while the epistemic reliability of each source is captured by a nonnegative weight $w_j^{(b)}$. In this manner, high-performing sources exert greater influence on the posterior, while less reliable sources are naturally down-weighted.

Given the Beta prior $\mathcal{B}(\alpha_{ij}, \gamma_{ij})$, the Bayesian update rule is expressed as [73]:

$$\begin{aligned} \alpha'_{ij} &= \alpha_{ij} + \sum_{b=1}^B w_j^{(b)} y_{ij}^{(b)} \\ \gamma'_{ij} &= \gamma_{ij} + \sum_{b=1}^B w_j^{(b)} (1 - y_{ij}^{(b)}) \end{aligned} \quad (12)$$

with posterior distribution:

$$P_{ij} | \text{data} \sim \mathcal{B}(\alpha'_{ij}, \gamma'_{ij}) \quad (13)$$

Posterior moments follow directly:

$$\begin{aligned} m'_{ij} &= \alpha'_{ij} / (\alpha'_{ij} + \gamma'_{ij}) \\ \zeta'_{ij} &= \alpha'_{ij} \gamma'_{ij} / \left((\alpha'_{ij} + \gamma'_{ij})^2 (\alpha'_{ij} + \gamma'_{ij} + 1) \right) \end{aligned} \quad (14)$$

Because the Beta update is associative and commutative, evidence from multiple sources or batches may be assimilated in any order. In this way, physics-based fragility priors are systematically refined by heterogeneous data streams, producing posterior distributions that coherently integrate structural knowledge and observational fidelity.

Figure 4 illustrates the first Bayesian updating stage. The PN prior derived from physics-based fragility (§2.1) is first mapped to a moment-matched Beta prior (§2.2.1) to enable conjugate updating with soft evidence from heterogeneous observation sources. After incorporating multi-fidelity observations (§2.2.2), the resulting Beta posterior is mapped back to the PN representation. This restores a latent fragility index form that remains fully compatible with the broader spatial and multi-output modeling framework introduced in §2.3. This cyclic mapping defines the local Bayesian update stage.

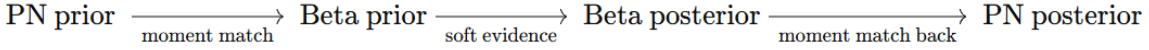


Figure 4: Local Bayesian Updating Cycle (PN–Beta–PN)

2.2.2.1. Calibration of Epistemic Weights

The epistemic weight $w_j^{(b)}$ introduced above quantifies the reliability of source b for predicting exceedance at threshold d_j . Whereas the soft exceedance probabilities $y_{ij}^{(b)}$ encode aleatory variability for each building i in the application dataset, the weights $w_j^{(b)}$ are derived from a designated evaluation subset of the application data. This ensures that the reliability factors reflect the observed performance of the source in the same operational domain in which the probabilistic scores are applied.

As an example, when source b is a machine learning model employed for computer-vision–based damage assessment, its reliability is quantified on labeled evaluation imagery. For each exceedance threshold d_j , $o_{\varsigma j} \in \{0,1\}$ denote the ground-truth indicator that sample ς from the evaluation subset satisfies $D \geq d_j$, while $g_{\varsigma j}^{(b)} \in (0,1)$ denote the predicted exceedance probability produced by source b for that event. Hence, the soft exceedance counts across evaluation samples ς are:

$$\begin{aligned}
TP_j^{(b)} &= \sum_{\varsigma} g_{\varsigma j}^{(b)} o_{\varsigma j} \\
FP_j^{(b)} &= \sum_{\varsigma} g_{\varsigma j}^{(b)} (1 - o_{\varsigma j}) \\
FN_j^{(b)} &= \sum_{\varsigma} (1 - g_{\varsigma j}^{(b)}) o_{\varsigma j}
\end{aligned} \tag{15}$$

where TP , FP , and FN denote the soft analogues of true positives, false positives, and false negatives, respectively. The resulting soft exceedance F1 score is defined as:

$$F1_j^{(b)} = 2TP_j^{(b)} / (2TP_j^{(b)} + FP_j^{(b)} + FN_j^{(b)}) \tag{16}$$

Finally, the soft F1 score is transformed into an epistemic reliability weight that ensures non-negativity, grows monotonically with predictive skill, and increases logarithmically as $F1_j^{(b)} \rightarrow 1$:

$$w_j^{(b)} = \log_2 \left(1 / (1 - F1_j^{(b)})^2 \right) \tag{17}$$

The transformation uses a squared gap $(1 - F1_j^{(b)})^2$ to impose a symmetric penalty on both precision and recall, consistent with the definition of the F1 score, and to produce a stricter separation between moderately accurate and highly accurate sources. Squaring also reduces the sensitivity of the reliability weight to sampling noise in F1 estimates. A base-2 logarithm is adopted so that the resulting weight is measured in information-theoretic units (bits), yielding the interpretable relationship $1 - F1 = 2^{-w/2}$, whereby each +2 units of weight correspond to halving the remaining prediction error.

2.3. Second Bayesian Stage: Global Spatial Propagation

Once local fragility indices are updated through the PN to Beta moment-matching procedure described in §2.2, the resulting estimates reflect building- and state-specific evidence with variances that differ substantially. This heterogeneity arises because some buildings may be observed immediately with high-fidelity data, while others may only be observed in the longer

term or with lower-quality information. As a result, some estimates exhibit small variances while others remain highly uncertain, producing strongly heteroscedastic posterior distributions.

The combination of this heteroscedasticity with the Gaussian structure induced by the probit transformation makes GPs a natural framework for the second stage of inference. Unlike ad hoc spatial interpolation, the GP provides a mathematically rigorous Bayesian posterior that remains fully tractable. It accommodates the varying reliability of local updates, weighting them according to their variance, and propagates information consistently across space, archetypes, and correlated damage states.

2.3.1. *Spatial Fragility Modeling Using a Probit-Warped Gaussian Process*

The PN marginals derived in §2.1 and updated with real-time data in §2.2 define, for each building i and damage state j , a fragility index in the probit space characterized by a mean μ_{ij} and variance σ_{ij}^2 . These quantities may originate purely from physics-based fragility functions or may incorporate data-driven updates when observations are available. In this study, these marginals are referred to as pseudo-observations, since they are not direct raw measurements but derived summaries of knowledge at each site. When high-fidelity data are available, the pseudo-observations carry small variances, whereas sparse or uncertain information yields large variances. This heteroscedastic structure naturally encodes differences in confidence across the building portfolio.

Formally, the GP observation model is expressed as

$$z_{ij} = Z(x_{ij}) + \epsilon_{ij}, \quad \epsilon_{ij} \sim \mathcal{N}(0, \sigma_{ij}^2) \quad (18)$$

where $z_{ij} = \mu_{ij}$, and σ_{ij}^2 is the associated variance. x_{ij} is the joint feature vector including spatial coordinates, structural archetype, and damage state. A zero-mean GP prior is then imposed on the latent fragility field:

$$Z(x) \sim \mathcal{GP}(0, K_t(x, x^*)) \quad (19)$$

where $K_t(x, x^*)$ is a composite kernel encoding structured dependencies across space, archetypes, and correlated damage states. x_{ij} denotes the structured input corresponding to the building-state pair (i, j) , including the spatial coordinates s_i , structural archetype a_i , and the ordinal damage-state index d_j . Detailed formulation of $K_t(x, x^*)$ is presented in §2.3.2.

Under this prior and likelihood, the marginal distribution of all fragility indices z_f is:

$$z_f \sim \mathcal{N}(0, \mathbf{K}_t + \Sigma_f) \quad (20)$$

where \mathbf{K}_t is the structured kernel matrix, and Σ_f is a diagonal matrix of heteroscedastic observation variances.

Conditioning on the pseudo-observations yields the exact GP posterior [74]:

$$\mu_{GP} = \mathbf{K}_t(\mathbf{K}_t + \Sigma_f)^{-1} z_f \quad (21)$$

$$\Sigma_{GP} = \mathbf{K}_t - \mathbf{K}_t(\mathbf{K}_t + \Sigma_f)^{-1} \mathbf{K}_t \quad (22)$$

The log-marginal likelihood of the data under this model is [75]:

$$\log p(z_f | \theta) = -0.5 z_f^\top (\mathbf{K}_t + \Sigma_f)^{-1} z_f - 0.5 \ln \det(\mathbf{K}_t + \Sigma_f) - 0.5 n_t \ln(2\pi) \quad (23)$$

where θ denotes kernel hyperparameters and $n_t = n_s n_d$ is the total number of building-state pairs.

From Equations (21 – 22), the noise covariance Σ_f dictates how observations interact and influence the posterior latent field. Within the matrix inversion term $(\mathbf{K}_t + \Sigma_f)^{-1}$, small diagonal entries in Σ_f amplify the corresponding precision weights, granting those observations stronger leverage in shaping the posterior mean. Conversely, large variances attenuate their influence, allowing the mean to remain closer to the prior expectation. Because the inversion operation couples all points through the kernel matrix \mathbf{K}_t , low-variance observations do not act in isolation—they anchor the surrounding latent field, pulling nearby high-variance predictions toward their own

mean values along the correlation structure defined by \mathbf{K}_t . This anchoring effect stabilizes the posterior field by transferring information from more reliable observations to uncertain regions. When multiple observations within a correlated neighborhood all exhibit low variance, the precision term becomes dominated by the kernel structure, causing the posterior mean to interpolate tightly between observed values and the posterior covariance Σ_{GP} to collapse locally; the field becomes highly data-driven, and the prior exerts minimal influence. In contrast, when all points in a region have high variance, the noise term Σ_f dominates, effectively decoupling the observations from one another and from the prior. In this regime, each data point contributes little to the posterior mean, which reverts toward the prior mean, while the posterior covariance remains close to the prior covariance.

While the exact posterior in Equations (21 – 22) is fully tractable, scalability becomes a bottleneck since matrix inversions scale cubically with the number of points n_t . To address this, a sparse variational GP approximation is adopted [76, 77]. By introducing a set of $n_{SV} \ll n_t$ inducing variables u at inducing points X_u , the posterior is approximated via a variational distribution:

$$q(u) = \mathcal{N}(\omega, \Upsilon) \quad (24)$$

with mean ω and covariance Υ . The evidence lower bound (ELBO) is then balancing data fit with divergence from the GP prior:

$$\text{ELBO}(\omega, \Upsilon, \theta) = \sum_{i=1}^{n_s} \sum_{j=1}^{n_d} \mathbb{E}_{q(Z(x_i))} [\ln p(z_{f,ij} | Z(x_{ij}))] - \text{KL}[q(u) \parallel p(u)] \quad (25)$$

The resulting approximate posterior takes the form:

$$\tilde{\mu}_{GP} = \mathbf{K}_{fu} \mathbf{K}_{uu}^{-1} \omega \quad (26)$$

$$\tilde{\Sigma}_{GP} = \mathbf{K}_{ff} - \mathbf{K}_{fu} \mathbf{K}_{uu}^{-1} (\mathbf{K}_{uu} - \Upsilon) \mathbf{K}_{uu}^{-1} \mathbf{K}_{fu}^\top \quad (27)$$

where \mathbf{K}_{ff} , \mathbf{K}_{fu} , and \mathbf{K}_{uu} denote kernel matrices over fragility sites, site-inducing cross-covariance, and inducing points, respectively. This formulation preserves the full Bayesian treatment of heteroscedastic noise while enabling efficient inference for large portfolios.

Finally, the GP posterior in probit space can be mapped analytically into probability space using Equations (6 – 8).

2.3.2. Composite Structured Kernel

The covariance structure imposed on the latent fragility field governs both the spatial coherence and the ordinal consistency of the probabilistic model. A single covariance component is insufficient to represent the dual nature of fragility behavior: large-scale dependencies arise from spatial and archetype-level similarities across the building portfolio, whereas fine-scale ordinal dependence characterizes the hierarchy of damage states within each individual structure. To capture these complementary relationships, a composite structured kernel is formulated, consisting of a global term that propagates information across space and archetype, and a local term that encourages ordinal and value-based coherence among damage states within the same building. The total covariance is expressed as

$$K_t((x_{ij}, z_{ij}), (x_{i^*j^*}, z_{i^*j^*})) = K_{\text{global}}(x_{ij}, x_{i^*j^*}) + K_{\text{local}}((x_{ij}, z_{ij}), (x_{i^*j^*}, z_{i^*j^*})) \quad (28)$$

2.3.2.1. Global correlations across buildings

The global covariance term K_{global} captures smooth variations of fragility across the regional building portfolio. It reflects broad correlations between buildings that are geographically close or structurally similar, while restricting these correlations to operate within identical damage states.

$$K_{\text{global}}(x_{ij}, x_{i^*j^*}) = \sigma_{\text{global}}^2 K_{\text{spatial}}(s_i, s_{i^*}) K_{\text{arch}}(a_i, a_{i^*}) K_{\text{state-global}}(d_j, d_{j^*}) \quad (29)$$

where σ_{global}^2 denotes the global marginal variance.

The spatial component K_{spatial} is modeled as a squared-exponential (RBF) kernel:

$$K_{\text{spatial}}(s_i, s_{i^*}) = \exp[-0.5(s_i - s_{i^*})^\top \Lambda^{-1}(s_i - s_{i^*})] \quad (30)$$

where s_i and s_{i^*} are spatial coordinates, and $\Lambda = \text{diag}(\ell_1^2, \ell_2^2)$ is the matrix of characteristic lengthscales. This component encodes the gradual spatial decay of correlation across the built environment.

The archetype component K_{arch} represents structural similarity between different building typologies:

$$K_{\text{arch}}(a_i, a_{i^*}) = \begin{cases} 1, & a_i = a_{i^*} \\ \rho_a, & a_i \neq a_{i^*} \end{cases} \quad (31)$$

where $\rho_a \in (0,1)$ quantifies the cross-archetype correlation and enables partial information transfer among different structural classes.

The global damage-state kernel is:

$$K_{\text{state-global}}(d_j, d_{j^*}) = \delta_{jj^*} \quad (32)$$

which ensures that correlations remain confined to identical damage thresholds. Consequently, the global term governs regional propagation of fragility patterns across space and archetype, but does not couple distinct damage states. This separation is particularly important for hazards that decay non-uniformly across damage thresholds, in which the intensity–damage relationship may vary significantly with severity. Without this restriction, the model would risk homogenizing all states near transitional intensity zones, effectively collapsing the probabilistic description into binary outcomes representing either no damage or complete collapse.

2.3.2.2. Local Ordinal and Value-Based Coherence

The damage states of a building represent progressively more severe outcomes of the same structural system, so their latent fragility indices should not be independent. Without additional structure, the GP would allow abrupt or unrealistic transitions among states within a building. The local kernel introduces a building-specific covariance across damage states that decreases as the

difference in their latent fragility indices grows. This encourages smooth, physically plausible transitions among states while allowing flexibility when states diverge. Because it operates only within each building, the local kernel supports internal coherence without affecting the spatial behavior determined by the global kernel.

Hence, a local covariance term K_{local} is introduced to encode structured dependence among damage states within each building. This term encourages ordinal smoothness in the latent domain and coherence across the full exceedance probability hierarchy. The local covariance is defined as:

$$K_{\text{local}}(x_{ij}, x_{i^*j^*}; z_{ij}, z_{i^*j^*}) = \sigma_{\text{local}}^2 \mathbb{I}\{i = i^*\} K_{\text{state-local}}(z_{ij}, z_{i^*j^*}) \quad (33)$$

where the indicator function $\mathbb{I}\{i = i^*\}$ confines this component to within-building correlations. The local variance is tied to the global scale by:

$$\sigma_{\text{local}}^2 = \alpha_{\text{local}} \sigma_{\text{global}}^2, \quad 0 < \alpha_{\text{local}} < 1 \quad (34)$$

so that the local component cannot dominate the posterior.

As defined earlier, z_{ij} denote the PN pseudo-observation mean index associated with the building i and damage state j . These values are fixed, deterministic quantities after the PN–Beta–PN update and therefore constitute valid input features for the GP. Hence, the kernel is defined as:

$$K_{\text{state-local}}(z_{ij}, z_{i^*j^*}) = \exp[-|z_{ij} - z_{i^*j^*}|/\tau], \quad \tau > 0 \quad (35)$$

where τ controls sensitivity to differences in the latent fragility field. Because this is the standard exponential (Matern– $\nu=0.5$) kernel applied to fixed real-valued inputs, it is positive semidefinite (PSD) and therefore admissible within the GP covariance structure. The kernel produces strong correlations between pseudo-observations whose PN means are close in magnitude and progressively weaker correlations as their latent indices diverge, ensuring that the fragility indices

evolve smoothly across adjacent damage thresholds while retaining flexibility for states positioned far apart in latent fragility space.

In practice, several pseudo-observation means may become numerically identical due to rounding, which can introduce near-duplicate rows in the kernel matrix. To preserve numerical stability, a vanishingly small perturbation is recommended to be added to the argument of the kernel, such as $\epsilon|j - j^*|$, where ϵ is a very small value, say $\epsilon \approx 10^{-8}$. This guarantees uniqueness without altering the kernel's theoretical PSD property or its practical behavior.

Because K_{local} is nonzero only when $i = i^*$, the resulting covariance matrix exhibits a block-Kronecker structure, in which each block corresponds to the intra-building covariance of damage states:

$$\mathbf{K}_{\text{local}} = \text{blockdiag}(\mathbf{K}_{\text{local}, i})_{i=1}^{n_s} \quad (36)$$

Each block $\mathbf{K}_{\text{local}, i}$ correlates the latent fragility indices $\{z_{ij}\}_{j=1}^{n_d}$ within building i . This structure preserves the natural ordering of exceedance probabilities and prevents unphysical reversals of damage severity at the building level.

Combining the global and local components yields the complete covariance matrix:

$$\mathbf{K}_t = \sigma_{\text{global}}^2 (\mathbf{K}_{\text{spatial}} \circ \mathbf{K}_{\text{arch}}) \otimes \mathbf{K}_{\text{state-global}} + \sigma_{\text{local}}^2 \mathbf{K}_{\text{local}} \quad (37)$$

where \circ and \otimes denote the Hadamard and Kronecker products, respectively.

3. Application Study

To demonstrate the applicability and scalability of the proposed methodology, an application study was conducted using the Joplin testbed [78] subjected to the 2011 Joplin tornado [79]. Figure 5a shows the spatial distribution of building archetypes, revealing a densely built inventory of 17,290 buildings dominated by wood-frame residential structures, with other archetypes distributed across the city. The archetypes are described in Table 1. Figure 5b overlays the

historical tornado footprint and its Enhanced Fujita (EF) intensity contours. This strong spatial gradient in hazard intensity provides a rigorous test of the model’s ability to learn fragility fields under localized extreme loading. Figure 5c presents post-event NOAA remote-sensing imagery [80].

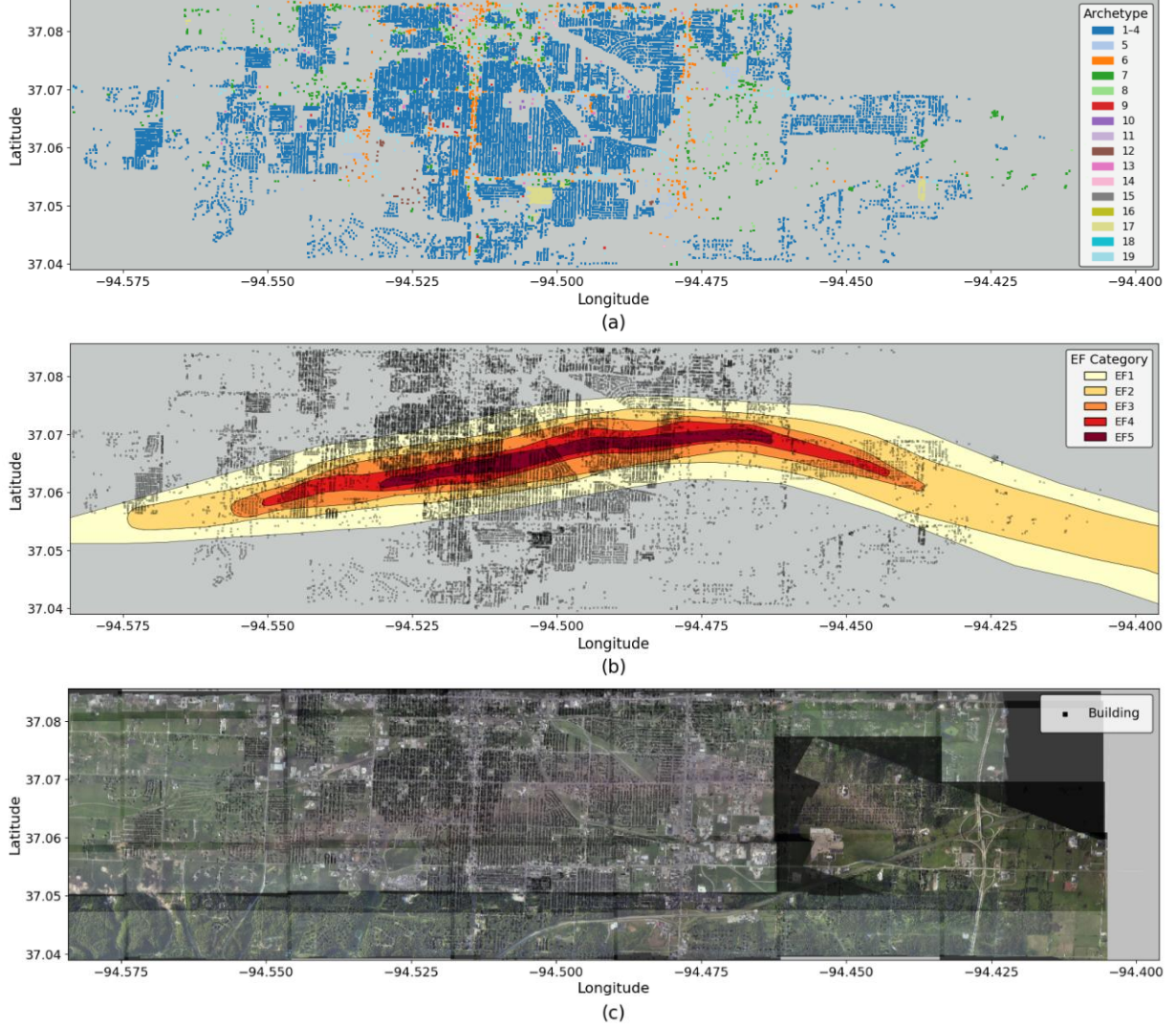


Figure 5: Maps showing (a) the spatial distribution of building archetypes, (b) EF intensity contours of the 2011 Joplin tornado obtained from IN-CORE [78], and (c) post-disaster remote-sensing imagery obtained from NOAA [80].

The remainder of this section is structured accordingly: §3.1 presents the development of the prior low-fidelity PN fragilities; §3.2 summarizes the computer-vision-based data used for updating; and §3.3 describes the experimental design and case-study comparisons.

3.1. Tornado Wind-Field Modeling for Prior Physics-Based Hazard Analysis

Prior hazard characterization was developed using a simplified Rankine-type vortex, modified to account for tornado horizontal translation. It is assumed that, immediately after the event, the track centerline of the tornado can be identified from rapid-sensing products. Using this centerline, each building's perpendicular distance to the tornado axis is computed in projected (meter) coordinates. The tornado is then represented as a slowly translating vortex whose wind intensity depends solely on radial distance from the centerline.

A total tornado width $W_{tornado}$ is prescribed to represent the full lateral extent of damaging winds. For an EF5 tornado, historical datasets [81] show that, on average, the EF5 core comprises approximately 27.3% of the total width, whereas the inner boundary of the EF0 region begins at about 87.3% of the total width. For the Joplin application, these percentages were adopted to define $R_{core} = 0.273W_{tornado}/2$ and $R_{edge} = 0.873W_{tornado}/2$, where R_{core} is the radius of the maximum-wind zone and R_{edge} marks the inner edge of the EF0 band. The corresponding wind speeds at these radii were taken as $V_{core} = 115 \text{ m/s}$, and $V_{edge} = 38 \text{ m/s}$. Historical data show that, for an EF5 tornado, the average width is 837m. However, because tornado width varies across events and along the track, $W_{tornado}$ was treated as a tunable parameter. Multiple scenarios were analyzed with different assumed widths; for each $W_{tornado}$, the implied R_{core} and R_{edge} , and their associated speeds were recomputed.

Let r denote the perpendicular distance from a site to the track centerline. The radial wind field is defined as:

$$V(r) = \begin{cases} V_{core} & , \quad r \leq R_{core} \\ V_{core}(R_{core}/r)^{\ln(V_{core}/V_{edge})/\ln(R_{edge}/R_{core})} & , \quad r > R_{core} \end{cases} \quad (38)$$

This power-law exponent enforces continuity between the EF5 core and the EF0 boundary, and the same decay is extended smoothly to the footprint boundary. Figure 6 shows the tornado wind field of various widths of 0, 400, 800, 1600, and 3200m.

It should be noted that the slow-translation, symmetric-vortex assumption is an intentional simplification. Real tornadoes exhibit right–left asymmetry due to translational motion and storm-relative inflow, but such information is typically unavailable immediately after a disaster. The symmetric Rankine-type vortex therefore serves as a pragmatic physics-based prior that is later refined through Bayesian updating using observed damage.

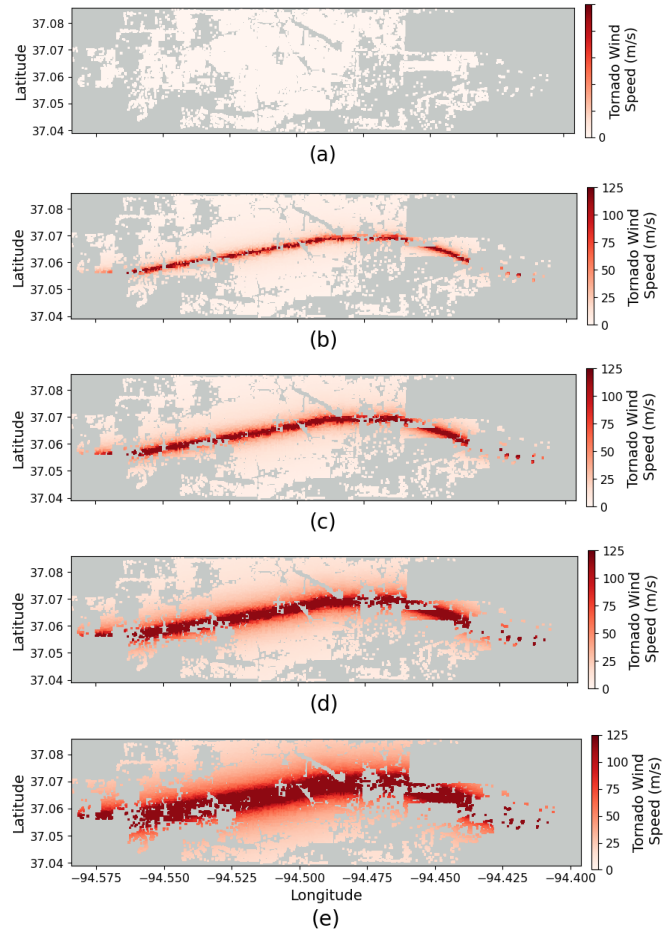


Figure 6: Maps showing the tornado wind field of various prior widths of (a) 0, (b) 400, (c) 800, (d) 1600, and (e) 3200m.

Using the constructed wind fields, lognormal fragility functions were applied to each building to compute damage-state exceedance probabilities and convert them into fragility indices in the probit space. The physics-based wind speeds were used as median capacity thresholds, and a dispersion of 0.09 was adopted, estimated from the expert-based variability reported in the original EF documentation [82]. The fragility parameters, summarized in Table 1, were drawn from prior studies on tornado performance [23, 29-31]. A logarithmic capacity dispersion of 0.40 was applied across all archetypes and damage states [83].

Table 1: Tornado fragility model parameters for building archetypes and damage states [23, 29-31].

Archetype	Damage State Description	Moderate		Extensive		Complete	
		Median (m/s)	Dispersion	Median (m/s)	Dispersion	Median (m/s)	Dispersion
1 - 4	Small to medium residential wood building	35.2	0.14	37.7	0.13	49.4	0.12
5	Large residential wood building	38.5	0.13	40.4	0.13	48.9	0.12
6	Strip mall	37.5	0.11	49.2	0.11	58.9	0.21
7	Light industrial building	40.2	0.1	44.0	0.1	47.7	0.1
8	Heavy industrial building	35.3	0.14	52.7	0.15	62.5	0.19
9	Elementary/middle school	42.3	0.11	49.2	0.1	65.0	0.12
10	High school	41.9	0.11	49.2	0.11	71.2	0.12
11	Fire/police station	49.2	0.12	57.1	0.12	65.7	0.19
12	Hospital	44.0	0.09	64.4	0.09	77.9	0.09
13	Community center/church	38.7	0.11	48.2	0.11	63.1	0.17
14	Government building	35.0	0.11	45.4	0.11	56.5	0.13
15	Large big-box	35.2	0.12	55.7	0.12	70.1	0.12
16	Small big-box	31.8	0.12	60.3	0.12	70.8	0.12
17	Mobile home	39.1	0.12	44.5	0.11	49.2	0.12
18	Shopping center	37.9	0.12	48.2	0.1	57.7	0.17
19	Office building	39.4	0.12	49.7	0.11	64.4	0.17

The resulting prior mean fragility indices quantify spatial vulnerability conditioned on the assumed tornado width. Figure 7 illustrates these prior fields for widths of 800 and 3200 m. For the 800m width (Figure 7a), large positive mean values, corresponding to high exceedance probability, are tightly concentrated near the track. For the 3200m scenario (Figure 7b), the high-fragility corridor becomes substantially broader. To ensure numerical stability and maintain ordinal progression across damage states, all latent probit means were clipped to $[-3,3]$. A value

of $|Z| = 3$ corresponds to probabilities of approximately 0.999 or 0.001, preventing the prior from expressing perfect certainty. When clipping occurred, a separation of 0.05 was imposed between successive damage states to preserve strict ordinality.

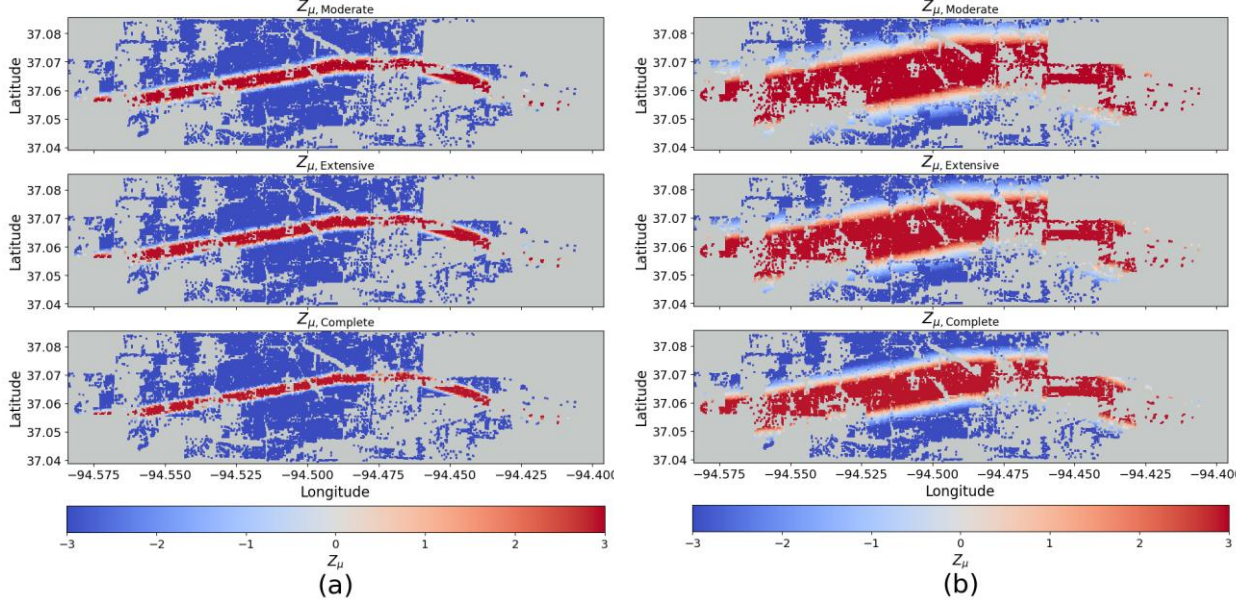


Figure 7: Spatial distribution of the prior physics-based mean fragility index in probit space for assumed tornado widths of (a) 800 m and (b) 3200 m.

Figure 8 presents corresponding expectations and variances in the probability space for the 800 m prior case. Expected exceedance probabilities follow the same spatial pattern as the probit means, but now lie within the $[0,1]$ interval. Variance peaks near the transition zone between damaged and undamaged regions, where wind speeds lie near each damage-state threshold, and becomes small inside the core and far from the track.

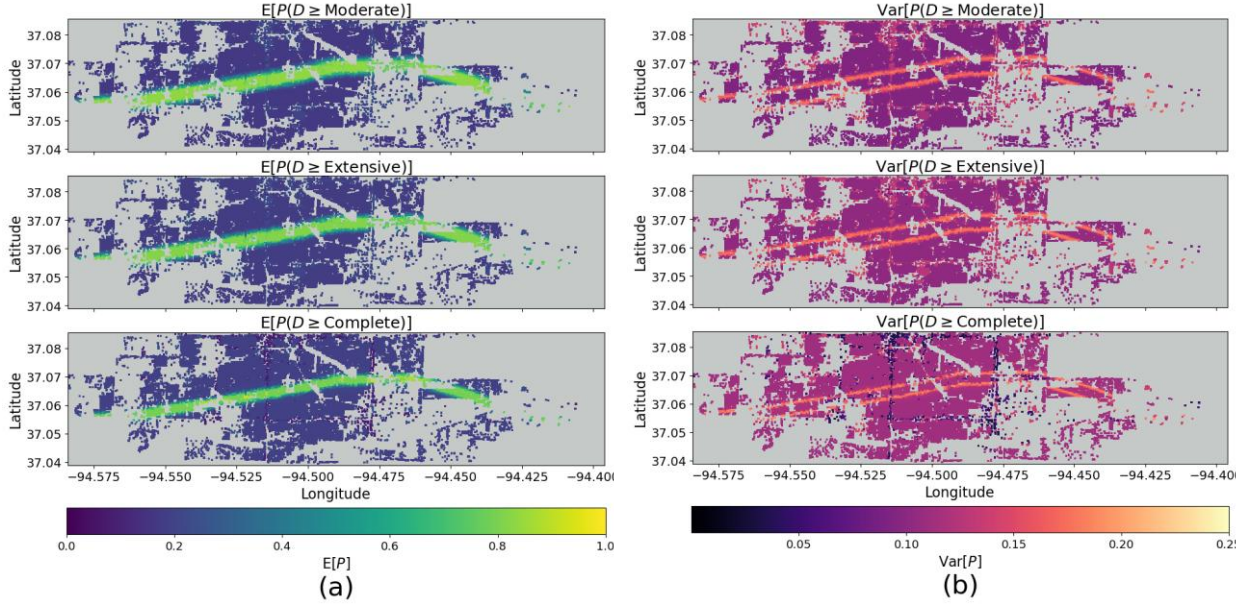


Figure 8: Spatial distribution of the prior fragility probabilities (transformed to probability space) for an assumed tornado width of 800 m: (a) expectation and (b) variance.

3.2. Updating with Computer-Vision-Based Damage Observations

Damage classification was performed using a convolutional neural network (CNN) developed in a prior study by Braik and Koliou [61]. The model was trained using the xBD dataset [84] together with manually curated sub-images extracted from several NOAA post-disaster events (excluding Joplin). Its architecture consisted of sequential convolution–pooling blocks, followed by fully connected layers and a SoftMax output layer producing probabilistic predictions for the HAZUS-consistent damage states of Moderate, Extensive, and Complete. Training relied on cross-entropy minimization with standard augmentation and validation procedures, and the model’s performance was evaluated using accuracy, precision, recall, F1-scores, and confusion matrices. In addition, the predictions were verified against historical post-Joplin damage observations. As the full development, training, and evaluation protocol has already been documented in Braik and Koliou [61], the reader is referred to that work for complete details.

The resulting soft confusion matrix and the exceedance-based confusion matrix are shown in Figure 9. The soft confusion matrix (Figure 9a) shows that the CNN reliably distinguishes between

adjacent damage states, with strong diagonal values and limited confusion between low and high damage levels. When evaluated in terms of exceedance (Figure 9b), performance shows consistently high probabilities, reflecting the model’s strength in identifying exceedance damage states.

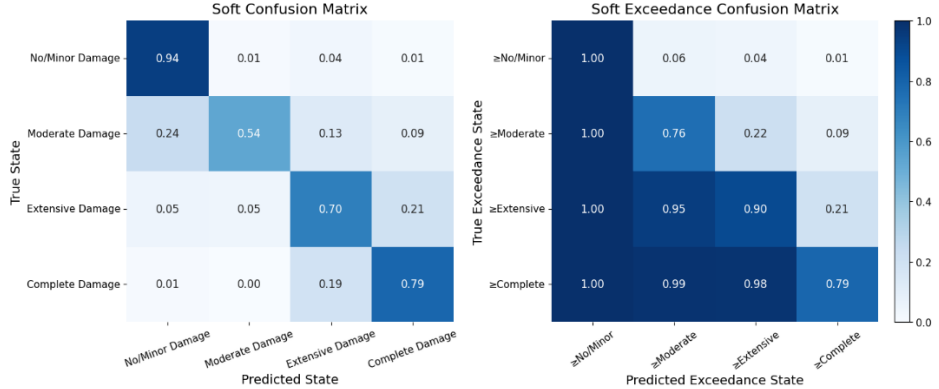


Figure 9: Soft confusion matrix and soft exceedance confusion matrix for the CNN-based tornado damage classifier.

The corresponding soft exceedance F1-scores and reliability weights (Table 2) confirm this pattern, with all thresholds providing meaningful probabilistic information for Bayesian updating. Overall, the resulting weights remain sufficiently large to ensure that the CNN contributes substantively and coherently within the multi-fidelity Bayesian updating framework.

Table 2: Soft exceedance F1-scores and information weights for each damage state.

Damage State	Soft $F1_j$	w_j
Moderate	0.90	6.68
Extensive	0.89	6.49
Complete	0.78	4.43

3.3. Experimental Design

The experiment was designed to assess how the proposed online Bayesian framework responds to incrementally arriving computer-vision evidence. The full building inventory was randomly divided into an 80% observed subset and a 20% holdout unobserved subset in a way that avoids spatial or structural bias. Only the observed buildings were included in the sequential updates, whereas the holdout buildings remained unchanged until the final step and were used solely for

validation. Within the observed subset, CNN soft predictions were released in eight batches generated under two sampling strategies. Random sampling produced spatially scattered updates that mimic distributed reconnaissance. In contrast, grouped sampling relied on spatial K-means clustering with enforced cluster sizes to create geographically coherent batches.

To examine how the strength of the physical prior influences the updating process, prior fragility predictions were initialized using five possible tornado wind-field widths: 0, 400, 800, 1600, and 3200 m. At each batch, the Bayesian update was performed in two modes. In the first mode, only the buildings in the incoming batch were updated, reflecting a strictly local assimilation strategy. In the second mode, the GP was used to reshape the latent fragility field so that new evidence propagated spatially and structurally to all buildings, including those that had not yet received direct CNN predictions.

Model performance after each batch was evaluated using the log-loss across the Moderate, Extensive, and Complete exceedance thresholds. Log-loss is a strictly proper scoring rule that penalizes miscalibrated probabilities, making it well-suited for assessing how closely the updated fragility predictions align with the CNN-derived soft evidence. Lower values correspond to better calibration relative to the available CNN information. It is important to note that all log-loss values were computed relative to the CNN soft probabilities, not ground-truth labels. The experiment, therefore, evaluates how effectively the framework assimilates the available evidence, not its accuracy in predicting true damage states.

4. Results and Discussion

4.1. *Predictive Accuracy and Convergence*

Figure 10 shows the log-loss trajectories for both observed and unobserved buildings across the three damage states. Initial loss values reflect the assumed prior wind-field width: the 800 m and

1600 m priors start closest to the CNN evidence, followed by 400 m, while 0 m and 3200 m begin with noticeably higher error. This ordering aligns with the average EF5 width of roughly 837 m [85] and confirms that priors closer to this scale yield more calibrated initial predictions.

For the observed buildings, log-loss decreases steadily as batches of soft evidence are assimilated. The local Bayesian update reliably improves fragility estimates, and the sampling strategy has little effect on these curves, since improvements occur almost entirely at locations receiving direct observations.

The unobserved buildings provide a clearer test of GP propagation. Because they receive no direct evidence until the final batch, their early behavior depends entirely on how well the GP transfers information from the observed subset. Across all prior widths and sampling strategies, GP-enabled runs show consistent loss reduction despite the absence of local updates, indicating that the spatial-archetype kernel effectively diffuses local corrections into unobserved regions.

Sampling strategy matters more strongly for the unobserved subset. Under random sampling, evidence appears throughout the domain during each batch, allowing the GP to deliver smooth, widespread improvements. Under grouped sampling, updates are confined to a single region at a time, causing unobserved areas far from the updated clusters to improve more slowly until nearby evidence becomes available.

After the dashed vertical line, when unobserved buildings finally receive their first direct CNN predictions, the contrast between methods is clear. Local (non-GP) runs experience a sharp drop in loss because these buildings have remained identical to the prior until that moment. In GP runs, the curves change very little, demonstrating that most corrections had already been inferred and propagated before any local evidence arrived.

Across all priors, sampling strategies, and damage states, both observed and unobserved buildings converge to essentially identical final log-loss values once all evidence is assimilated. This convergence shows that prior hazard width and sampling order influence only the early data-scarce regime; with sufficient observations, the posterior is dominated by the available evidence and the GP’s structured spatial–archetype correlations.

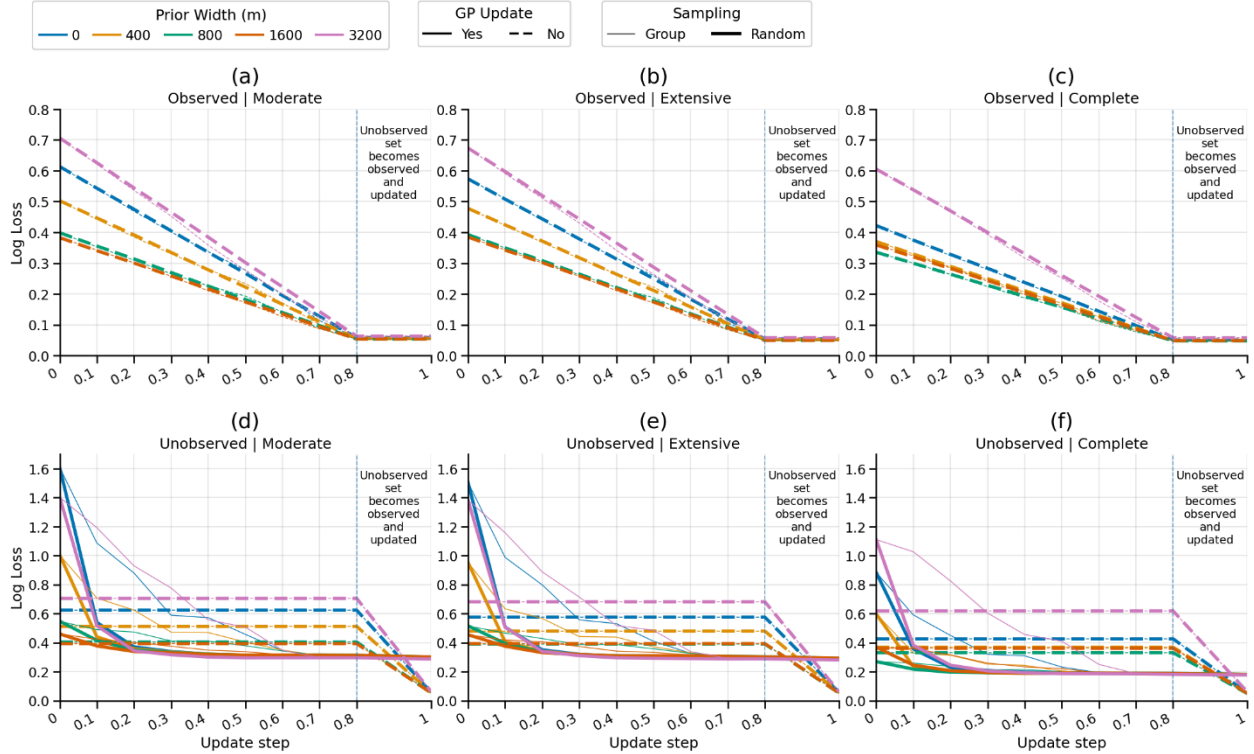


Figure 10: Log-loss evolution across update steps for observed (panels a–c) and unobserved (panels d–f) buildings. Columns correspond to the Moderate, Extensive, and Complete damage states, respectively. Results are shown under varying prior widths, sampling strategies, and with and without GP propagation.

4.2. Spatial Reconstruction and Uncertainty Quantification

Figure 11 illustrates how the GP reconstructs the fragility field for unobserved buildings as CNN evidence is incrementally assimilated for the Extensive damage state, under the 0-m prior width, where the prior contains no spatial structure. At 0% updates, both sampling strategies produce a nearly uniform zero-probability field, reflecting the absence of a physics-based gradient. Under random sampling (Figure 11a), spatially dispersed evidence allows the GP to rapidly

introduce high-fidelity corrections throughout the domain; the tornado corridor becomes visible as early as 10–20% updates, and by 40%, the field closely resembles the true damage pattern due to efficient propagation across space and archetypes. Under grouped sampling (Figure 11b), early updates remain confined to the initial spatial cluster, producing strong local corrections while leaving the rest of the building portfolio unchanged at 10–20%. Only after later batches (80%) do these localized updates expand and merge into a coherent damage corridor. The 100% update corresponds to the moment when the previously unobserved buildings finally receive their own CNN-based pseudo-observations. As observed earlier in Figure 10, the GP has already driven the unobserved buildings extremely close to their final values before this point; the direct observations therefore produce only minor adjustments, and the two sampling strategies arrive at nearly identical spatial fields once the full data set is assimilated.

Figure 12 illustrates how the posterior exceedance probabilities and their associated uncertainties evolve for the Extensive damage state under an exaggerated prior tornado width of 3200 m, using random sampling. Panel (a) presents the expected exceedance probability for the unobserved buildings only, while panel (b) displays the heteroscedastic variance for all buildings, allowing the behavior of high- and low-fidelity subsets to be distinguished.

Because the 3200 m prior assumes an unrealistically wide tornado, the initial 0% field in Figure 12a shows high exceedance probabilities almost everywhere. As CNN evidence is incrementally assimilated (10–20%), the GP rapidly corrects these inflated predictions outside the true damage corridor and reconstructs a much narrower, data-consistent pattern. By 40%, the posterior field is shaped almost entirely by the PN–Beta updates and GP propagation, effectively overriding the mis-specified prior and restoring a realistic gradient aligned with the tornado path.

The corresponding variance fields in Figure 12b show how this correction develops. Initially, the variance is large throughout the region, reflecting the method’s acknowledgment that the prior provides very little reliable information. As updates accumulate, variance drops sharply around buildings that have received CNN-based pseudo-observations and remains high elsewhere. By 80%, the map clearly separates regions that have been updated from those that have not.

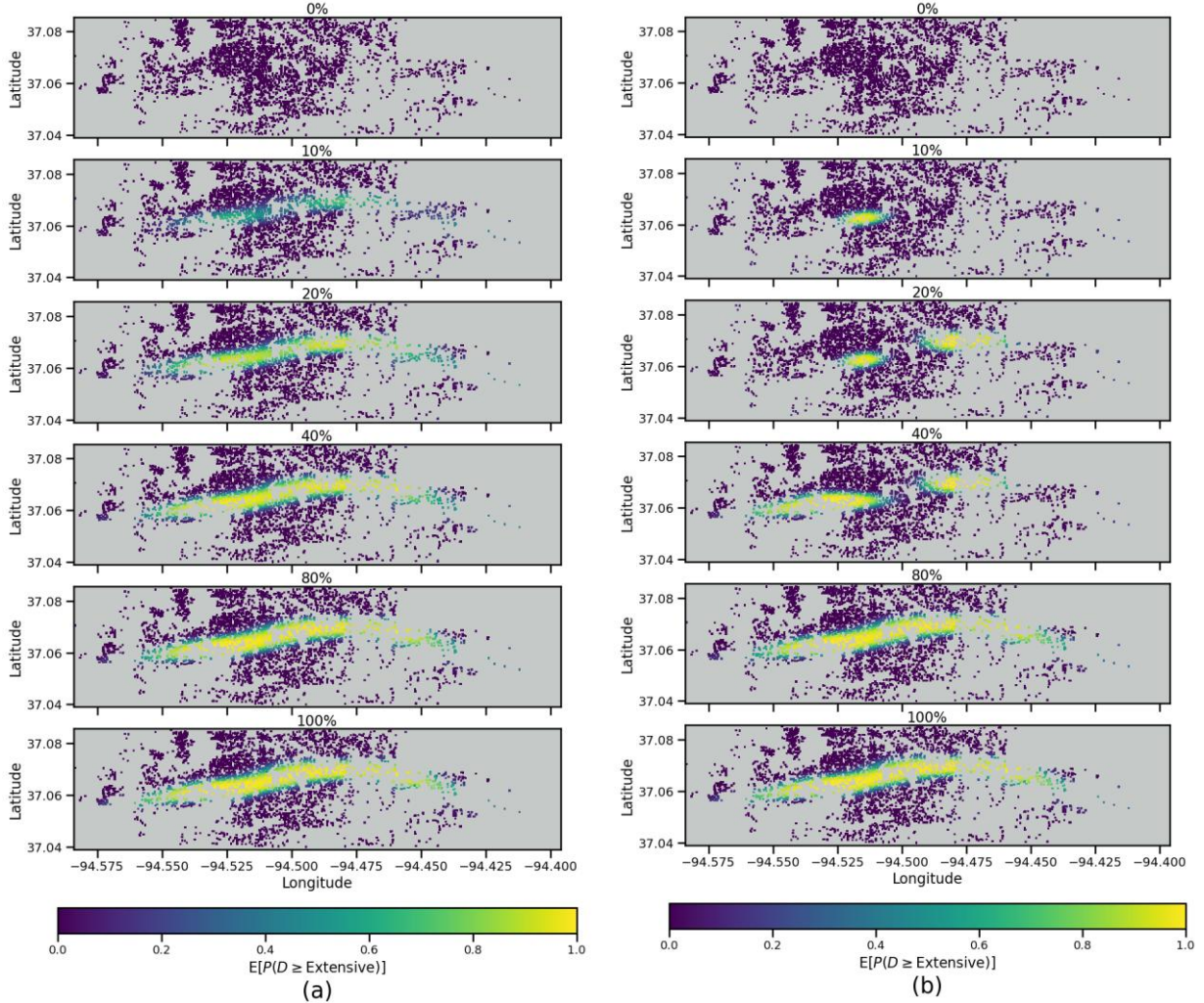


Figure 11: Incremental GP-based reconstruction of the Extensive-damage fragility field for unobserved buildings under the 0-m prior width, shown for random sampling (a) and grouped sampling (b).

At 100%, all buildings have been updated, and the remaining variance pattern is driven by both archetype and spatial position. An interesting feature appears along the edges of the reconstructed damage corridor: variance becomes higher near the boundaries. This occurs because the

exceedance probabilities in these transition zones sit near the steepest part of the probit link, where small changes in the latent fragility index lead to large differences in probability.

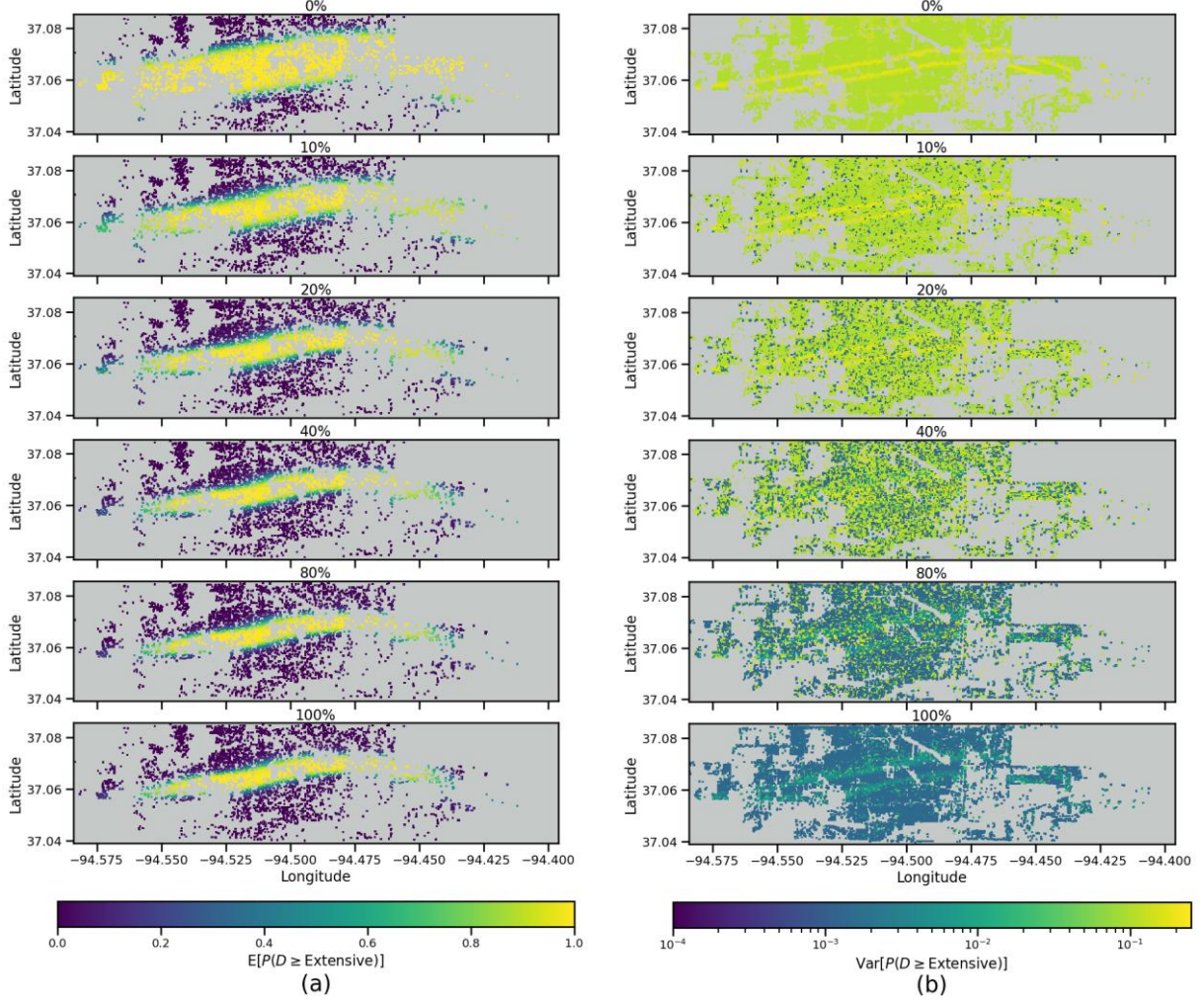


Figure 12: Evolution of the posterior exceedance field for the Extensive damage state under an exaggerated 3200 m prior tornado width with random sampling. Panel (a) shows the expected exceedance probability for the unobserved buildings only, and panel (b) shows the corresponding variance for all buildings, at cumulative update levels of 0%, 10%, 20%, 40%, 80%, and 100%.

Figure 13 shows the distribution of posterior variance across all three damage states at the 80 percent update level, when 80 percent of buildings have already received CNN-based pseudo-observations and the remaining 20 percent are still unobserved. Figure 13b corresponds directly to the 80% variance map shown in Figure 12b. Across all states, the variance distributions clearly separate the observed and unobserved buildings. Observed buildings show substantially smaller

variance. This reflects the fact that these buildings have transitioned to high-fidelity estimates that strongly constrain the GP posterior. Unobserved buildings retain much larger variance because their predictions depend entirely on GP propagation from neighboring sites.

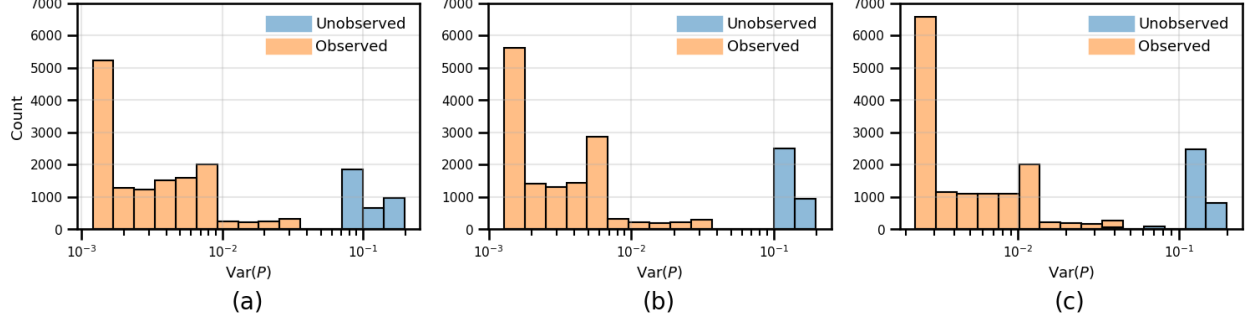


Figure 13: Posterior variance ($\text{Var}(P)$) distributions for observed versus unobserved buildings for the (a) Moderate, (b) Extensive, and (c) Complete damage states.

4.3. Hyperparameter Evolution and Kernel Interpretation

Figure 14 illustrates the evolution of the GP hyperparameters as incremental batches of pseudo-observations are assimilated. The archetype correlation parameter (Figure 14a) converges rapidly to a tight interval around 0.87–0.89 across all prior widths and sampling strategies. This indicates strong, but not complete, similarity among structural archetypes under an EF5 tornado, consistent with a hazard-governed spatial damage regime.

The spatial lengthscales reflect a stable anisotropy that remains identifiable across scenarios. The longitude lengthscale (Figure 14c) converges to a larger and consistently narrow-bound interval (≈ 0.64), indicating dominant data-driven control in the along-track direction, with minimal residual influence from the initial priors. The latitude lengthscale (Figure 14b) also converges quickly to meaningful values (≈ 0.33 –0.39), showing only moderate variation across scenarios, consistent with a limited but expected sensitivity to the early prior settings in the perpendicular direction.

Similarly, the variance parameters exhibit differentiated learning responses. The global variance (Figure 14d) retains notable influence from its originating prior width assumptions,

indicating that global uncertainty estimation is still partially guided by initial kernel scale choices. In contrast, the local-to-global variance ratio (Figure 14e) stabilizes to a bounded interval of 0.15–0.25, confirming that ordinal relationships between damage states contribute to the uncertainty structure but do not govern it.

Notably, the spatial and archetype correlation hyperparameters converge to stable, data-driven values that remain physically meaningful and learnable, while variance kernel scales retain moderate, interpretable sensitivity to early model assumptions without limiting learning. Overall, the kernel evolves toward a predominantly data-governed representation of spatial and archetype coherence, while remaining consistent with physical expectations.

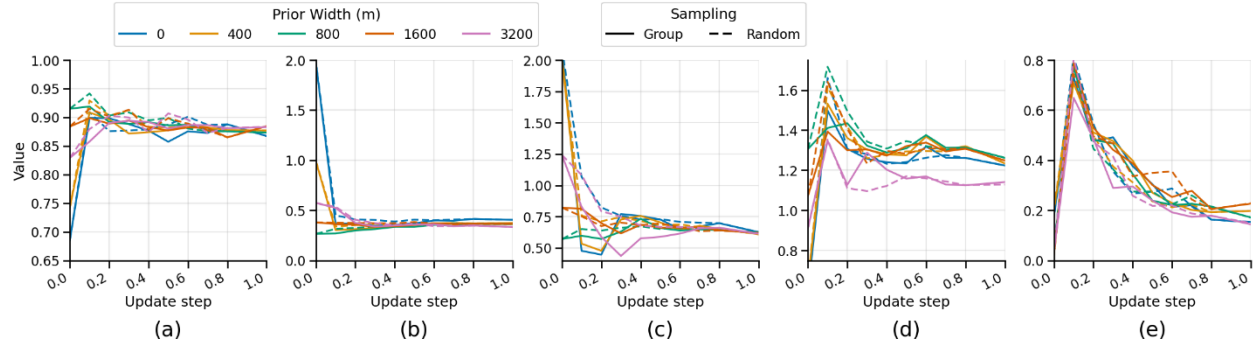


Figure 14: Evolution of GP hyperparameters across incremental updates for varying prior widths and sampling strategies: (a) archetype correlation ρ_a , (b) ℓ_1 (latitude), (c) ℓ_2 (longitude), (d) σ_{global}^2 , and (e) α_{local} .

4.4. Computational Efficiency

All analyses were conducted in Python and executed on a desktop equipped with 64 GB of RAM and a 12th-generation Intel Core i7-12700 CPU running at 2.1 GHz. All analysis steps—including prior hazard and fragility construction, PN formulation, PN–Beta moment matching, and conjugate Beta updating—were coded from scratch using general Python libraries such as NumPy, GeoPandas, and SciPy. GP hyperparameter optimization was performed using the GPyTorch library [86]. For a dataset containing 17,290 buildings and 3 damage states, each updating step,

consisting of both local updating and global GP training, completed in around 5 minutes, demonstrating the computational scalability of the two-stage Bayesian online framework.

5. Conclusions and Future Work

This study introduced a mathematically grounded, fully Bayesian two-stage online learning framework for regional fragility fields, integrating physics-based priors with heterogeneous post-disaster observations in a coherent probabilistic methodology. The framework begins by reformulating physics-based fragility functions into a PN representation that embeds aleatory variability and epistemic uncertainty within a single, analytically tractable latent index. In the first Bayesian stage, each PN marginal is moment-matched to a Beta surrogate, enabling exact conjugate updating of soft exceedance observations with source-specific reliability weights while preserving the mean, variance, and statistical shape of the original PN model. In the second Bayesian stage, the updated PN parameters are assimilated into a probit-warped GP with structured global and local kernels, allowing information to propagate across space, archetypes, and correlated damage states. This produces a spatially coherent, uncertainty-aware fragility field with closed-form exceedance probabilities. A central methodological contribution is showing that the PN–Beta surrogate provides an almost lossless approximation that preserves the physical interpretability and Gaussian structure of PN while enabling analytically tractable online updating, keeping the two-stage Bayesian system both rigorous and scalable.

The application to the 2011 Joplin tornado provided a detailed empirical assessment across more than 17,000 buildings. Initial fragility fields were strongly influenced by the assumed tornado width, but this sensitivity diminished steadily as CNN-derived exceedance probabilities were assimilated. All prior widths, including the extreme 0 m and 3200 m scenarios, converged toward nearly identical performance once sufficient evidence accumulated. Local updating consistently

reduced log-loss for directly observed buildings, while the GP facilitated systematic knowledge sharing across the region. Unobserved buildings improved steadily throughout the update sequence and required only minor adjustments once their observations arrived, indicating that most corrections had already been inferred through spatial and archetype-level propagation.

Spatial probability and variance maps reinforced these findings: under the 0 m prior, the GP reconstructed the tornado corridor purely from the spatial pattern of evidence, while under the 3200 m prior it rapidly suppressed unrealistic probabilities outside the corridor and restored a data-consistent gradient after only a few batches. Variance patterns showed clear stratification, with uncertainty collapsing around high-fidelity observations and remaining elevated in data-scarce regions. The hyperparameter trajectories offered further insight into the learned structure. Parameters linked to strong, well-identified physical gradients, such as the archetype correlation and the spatial lengthscale perpendicular to the tornado path, converged consistently across all scenarios.

Several directions for future work remain. The framework could be extended to multi-hazard contexts in which interactions between wind and flood, or between seismic and tsunami effects, require joint fragility modeling. Additional observational modalities, including crowd-sourced imagery and sensor networks, may be incorporated with learned reliability weights. Alternative kernel structures may improve performance in complex urban environments. Embedding the framework within operational digital twins would enable continuous updating of fragility fields and more transparent integration with response, recovery, and long-term resilience planning. Moreover, a more definitive validation will require large-scale ground truth labels.

In summary, this study provides one of the first integrated demonstrations of a physics-informed, data-assimilative fragility modeling system at the regional scale. The results show that

fragility modeling can move beyond static, pre-event curves toward dynamic systems that evolve as evidence accumulates. The framework illustrates how such systems can operate in practice and how they can support real-time adaptive digital twins that learn from new observations. Continued development in this direction may significantly enhance the speed, transparency, and reliability of post-disaster decision making.

Declaration of competing interests

The authors declare that they have no known competing financial interests or personal relationships that could have appeared to influence the work reported in this paper.

Acknowledgments

Partial financial support for this study was provided by the US National Science Foundation (NSF) under Award Number 2052930. This financial support is gratefully acknowledged. Any opinions, findings, conclusions, and recommendations presented in this paper are those of the authors and do not necessarily reflect the views of NSF.

References

- [1] Cornell CA. Bounds on the reliability of structural systems. *Journal of the Structural Division*. 1967;93:171-200.
- [2] Ang AH. Structural risk analysis and reliability-based design. *Journal of the Structural Division*. 1973;99:1891-910.
- [3] Ang AH, Cornell CA. Reliability bases of structural safety and design. *Journal of the structural division*. 1974;100:1755-69.
- [4] Ellingwood B. Development of a probability based load criterion for American National Standard A58: Building code requirements for minimum design loads in buildings and other structures: US Department of Commerce, National Bureau of Standards; 1980.
- [5] Kennedy R, Short SA. Basis for seismic provisions of DOE-STD-1020. Lawrence Livermore National Lab. (LLNL), Livermore, CA (United States ...; 1994.
- [6] Kircher CA, Nassar AA, Kustu O, Holmes WT. Development of building damage functions for earthquake loss estimation. *Earthquake spectra*. 1997a;13:663-82.
- [7] Kircher CA, Reitherman RK, Whitman RV, Arnold C. Estimation of earthquake losses to buildings. *Earthquake spectra*. 1997b;13:703-20.
- [8] FEMA. HAZUS technical manual. National Institute of Building for the Federal Emergency Management Agency, Washington (DC). 1997.
- [9] Koliou M, van de Lindt JW, McAllister TP, Ellingwood BR, Dillard M, Cutler H. State of the research in community resilience: Progress and challenges. *Sustainable and resilient infrastructure*. 2020;5:131-51.
- [10] Burton H, Rad AR, Yi Z, Gutierrez D, Ojuri K. Seismic collapse performance of Los Angeles soft, weak, and open-front wall line woodframe structures retrofitted using different procedures. *Bulletin of earthquake engineering*. 2019;17:2059-91.

[11] Choe D-E, Gardoni P, Rosowsky D, Haukaas T. Probabilistic capacity models and seismic fragility estimates for RC columns subject to corrosion. *Reliability Engineering & System Safety*. 2008;93:383-93.

[12] Ramamoorthy SK, Gardoni P, Bracci JM. Probabilistic demand models and fragility curves for reinforced concrete frames. *Journal of structural Engineering*. 2006;132:1563-72.

[13] Gardoni P, Der Kiureghian A, Mosalam KM. Probabilistic capacity models and fragility estimates for reinforced concrete columns based on experimental observations. *Journal of Engineering Mechanics*. 2002;128:1024-38.

[14] Qiu C-X, Zhu S. Performance-based seismic design of self-centering steel frames with SMA-based braces. *Engineering Structures*. 2017;130:67-82.

[15] Li Y, Song R, Van De Lindt JW. Collapse fragility of steel structures subjected to earthquake mainshock-aftershock sequences. *Journal of Structural Engineering*. 2014;140:04014095.

[16] Cornell CA, Jalayer F, Hamburger RO, Foutch DA. Probabilistic basis for 2000 SAC federal emergency management agency steel moment frame guidelines. *Journal of structural engineering*. 2002;128:526-33.

[17] Rosowsky DV, Ellingwood BR. Performance-based engineering of wood frame housing: Fragility analysis methodology. *Journal of Structural Engineering*. 2002;128:32-8.

[18] Ellingwood BR, Rosowsky DV, Li Y, Kim JH. Fragility assessment of light-frame wood construction subjected to wind and earthquake hazards. *Journal of structural engineering*. 2004;130:1921-30.

[19] Filiatrault A, Sullivan T. Performance-based seismic design of nonstructural building components: The next frontier of earthquake engineering. *Earthquake Engineering and Engineering Vibration*. 2014;13:17-46.

[20] Vamvatsikos D, Cornell CA. Incremental dynamic analysis. *Earthquake engineering & structural dynamics*. 2002;31:491-514.

[21] Abdelhady AU, Spence SM, McCormick J. Risk and fragility assessment of residential wooden buildings subject to hurricane winds. *Structural Safety*. 2022;94:102137.

[22] Li Y, Ellingwood BR. Hurricane damage to residential construction in the US: Importance of uncertainty modeling in risk assessment. *Engineering structures*. 2006;28:1009-18.

[23] Memari M, Attary N, Masoomi H, Mahmoud H, van de Lindt JW, Pilkington SF et al. Minimal building fragility portfolio for damage assessment of communities subjected to tornadoes. *Journal of Structural Engineering*. 2018;144:04018072.

[24] Nofal OM, van de Lindt JW. Fragility-based flood risk modeling to quantify the effect of policy change on losses at the community level. *Civ Eng Res J*. 2021;11:555822.

[25] van de Lindt JW, Taggart M. Fragility analysis methodology for performance-based analysis of wood-frame buildings for flood. *Natural Hazards Review*. 2009;10:113-23.

[26] Nofal OM, van de Lindt JW, Do TQ. Multi-variate and single-variable flood fragility and loss approaches for buildings. *Reliability Engineering & System Safety*. 2020;202:106971.

[27] Tomiczek T, Kennedy A, Rogers S. Collapse limit state fragilities of wood-framed residences from storm surge and waves during Hurricane Ike. *Journal of Waterway, Port, Coastal, and Ocean Engineering*. 2014;140:43-55.

[28] Do TQ, van de Lindt JW, Cox DT. Hurricane surge-wave building fragility methodology for use in damage, loss, and resilience analysis. *Journal of structural engineering*. 2020;146:04019177.

[29] Masoomi H, van de Lindt JW. Tornado fragility and risk assessment of an archetype masonry school building. *Engineering Structures*. 2016;128:26-43.

[30] Koliou M, Masoomi H, van de Lindt JW. Performance assessment of tilt-up big-box buildings subjected to extreme hazards: Tornadoes and earthquakes. *Journal of Performance of Constructed Facilities*. 2017;31:04017060.

[31] Masoomi H, Ameri MR, van de Lindt JW. Wind performance enhancement strategies for residential wood-frame buildings. *Journal of Performance of Constructed Facilities*. 2018;32:04018024.

[32] Padgett JE, DesRoches R. Methodology for the development of analytical fragility curves for retrofitted bridges. *Earthquake Engineering & Structural Dynamics*. 2008;37:1157-74.

[33] Nie Y, Li J, Liu G, Zhou P. Cascading failure-based reliability assessment for post-seismic performance of highway bridge network. *Reliability Engineering & System Safety*. 2023;238:109457.

[34] Ma X, Xiong W, Zhou D, Cai C. Fragility analysis of multiple bridges under scour conditions enabled by knowledge transferred from single bridge. *Reliability Engineering & System Safety*. 2025;111837.

[35] Braik AM, Salman AM, Li Y. Risk-based reliability and cost analysis of utility poles subjected to tornado hazard. *Journal of Aerospace Engineering*. 2019;32:04019040.

[36] Li Y, Salman AM, Braik A, Bjarnadóttir S, Salarieh B. Risk-Based Management of Electric Power Distribution Systems Subjected to Hurricane and Tornado Hazards. *Engineering for Extremes: Decision-Making in an Uncertain World*: Springer; 2021. p. 143-66.

[37] Salman AM, Li Y, Bastidas-Arteaga E. Maintenance optimization for power distribution systems subjected to hurricane hazard, timber decay and climate change. *Reliability Engineering & System Safety*. 2017;168:136-49.

[38] Zhang J, Bagtzoglou Y, Zhu J, Li B, Zhang W. Fragility-based system performance assessment of critical power infrastructure. *Reliability Engineering & System Safety*. 2023;232:109065.

[39] Farahmandfar Z, Piratla KR, Andrus RD. Resilience evaluation of water supply networks against seismic hazards. *Journal of Pipeline Systems Engineering and Practice*. 2017;8:04016014.

[40] Zhang Y, Zhong Z, Li J, Hou B, Xu C. Experimental investigation and seismic performance assessment of cast iron pipelines considering the mechanical property uncertainties of cement-caulked joints. *Reliability Engineering & System Safety*. 2025;111625.

[41] FEMA. HAZUS-MHMR Methodology, Multi-hazard Loss Estimation. Technical Manual, NIST, Washington, DC. 2003.

[42] FEMA. Seismic Performance Assessment of Buildings, Volume 1 – Methodology. FEMA P-58-1, prepared by the Applied Technology Council (ATC) for the Federal Emergency Management Agency. 2012.

[43] Braik AM, Gupta HS, Koliou M, González AD. Multi - hazard probabilistic risk assessment and equitable multi - objective optimization of building retrofit strategies in hurricane - vulnerable communities. *Computer - Aided Civil and Infrastructure Engineering*. 2025.

[44] Aghababaei M, Koliou M, Paal SG. Performance assessment of building infrastructure impacted by the 2017 Hurricane Harvey in the Port Aransas region. *Journal of Performance of Constructed Facilities*. 2018;32:04018069.

[45] Van de Lindt JW, Peacock WG, Mitrani-Reiser J, Rosenheim N, Deniz D, Dillard M et al. Community resilience-focused technical investigation of the 2016 Lumberton, North Carolina, flood: An interdisciplinary approach. *Natural Hazards Review*. 2020;21:04020029.

[46] Aghababaei M, Okamoto C, Koliou M. Examining the accuracy and validity of loss estimations using the PBEE methodology for wood residential buildings through integrated experimental findings and expert panel solicitation. *Sustainable and Resilient Infrastructure*. 2022;7:638-54.

[47] van de Lindt JW, Wang WL, Johnston B, Crawford PS, Yan G, Dao T et al. Social Susceptibility–Driven Longitudinal Tornado Reconnaissance Methodology: 2021 Midwest Quad-State Tornado Outbreak. *ASCE OPEN: Multidisciplinary Journal of Civil Engineering*. 2025;3:04025006.

[48] Merhi A, Brown-Giannanco TM, Roueche DB, Wood RL, Murphy TA, Standohar-Alfano CD et al. Damage Assessment of the 2020 Monroe, Louisiana, Tornado Using Different Remote-Sensing Methods and Enhanced Fujita Scales. *Natural Hazards Review*. 2026;27:04025062.

[49] Matin SS, Pradhan B. Challenges and limitations of earthquake-induced building damage mapping techniques using remote sensing images-A systematic review. *Geocarto International*. 2022;37:6186-212.

[50] Kaur N, Lee CC, Mostafavi A, Mahdavi - Amiri A. Large - scale building damage assessment using a novel hierarchical transformer architecture on satellite images. *Computer - Aided Civil and Infrastructure Engineering*. 2023.

[51] Kaur S, Gupta S, Singh S, Koundal D, Zaguia A. Convolutional neural network based hurricane damage detection using satellite images. *Soft Computing*. 2022;26:7831-45.

[52] Khajwal AB, Cheng CS, Noshadravan A. Post - disaster damage classification based on deep multi - view image fusion. *Computer - Aided Civil and Infrastructure Engineering*. 2023;38:528-44.

[53] Braik AM, Koliou M. Automated building damage assessment and large - scale mapping by integrating satellite imagery, GIS, and deep learning. *Computer - Aided Civil and Infrastructure Engineering*. 2024a;39, 2389 – 2404.

[54] Fan C, Jiang Y, Mostafavi A. Social sensing in disaster city digital twin: Integrated textual–visual–geo framework for situational awareness during built environment disruptions. *Journal of Management in Engineering*. 2020;36:04020002.

[55] Ford DN, Wolf CM. Smart cities with digital twin systems for disaster management. *Journal of management in engineering*. 2020;36:04020027.

[56] Ghosh S, Huyck CK, Greene M, Gill SP, Bevington J, Svekla W et al. Crowdsourcing for rapid damage assessment: The global earth observation catastrophe assessment network (GEO-CAN). *Earthquake Spectra*. 2011;27:179-98.

[57] Khajwal AB, Noshadravan A. An uncertainty-aware framework for reliable disaster damage assessment via crowdsourcing. *International Journal of Disaster Risk Reduction*. 2021;55:102110.

[58] Cheng C-S, Behzadan AH, Noshadravan A. Bayesian inference for uncertainty-aware post-disaster damage assessment using artificial intelligence. *Computing in Civil Engineering* 20212022. p. 156-63.

[59] Behrooz H, Ilbeigi M, Reisi-Gahrooei M. Adaptive Data Collection for Post-Disaster Rapid Damage Assessment: A Multi-Objective Optimization Approach. Available at SSRN 5274318.

[60] Huang S, Sun C, Gong J, Pompili D. Reinforcement learning – based task allocation and path - finding in multi - robot systems under environment uncertainty. *Computer - Aided Civil and Infrastructure Engineering*. 2025.

[61] Braik AM, Koliou M. Post-Tornado Automated Building Damage Evaluation and Recovery Prediction by Integrating Remote Sensing, Deep Learning, and Restoration Models. *Sustainable Cities and Society*. 2025b;106286.

[62] Braik AM, Han X, Koliou M. A Framework for Resilience Analysis and Equitable Recovery in Tornado-impacted Communities Using Agent-based Modeling and Computer Vision-based Damage Assessment. *International Journal of Disaster Risk Reduction*. 2025;105427.

[63] De Risi R, Goda K, Mori N, Yasuda T. Bayesian tsunami fragility modeling considering input data uncertainty. *Stochastic environmental research and risk assessment*. 2017;31:1253-69.

[64] Koutsourelakis PS. Assessing structural vulnerability against earthquakes using multi-dimensional fragility surfaces: A Bayesian framework. *Probabilistic Engineering Mechanics*. 2010;25:49-60.

[65] Braik AM, Koliou M. A novel digital twin framework of electric power infrastructure systems subjected to hurricanes. *International Journal of Disaster Risk Reduction*. 2023;97:104020.

[66] Braik AM, Koliou M. A digital twin framework for efficient electric power restoration and resilient recovery in the aftermath of hurricanes considering the interdependencies with road network and essential facilities. *Resilient Cities and Structures*. 2024c;3:79-91.

[67] Braik AM, Koliou M. Spatially Correlated Multi-State Fragility via a Warped Gaussian Process. *Structural Safety*. 2026;Under Review.

[68] Johnson NL, Kotz S, Balakrishnan N. *Continuous univariate distributions*, volume 2: John wiley & sons; 1995.

[69] MacKay DJ. *Information theory, inference and learning algorithms*: Cambridge university press; 2003.

[70] Cover TM. *Elements of information theory*: John Wiley & Sons; 1999.

[71] van de Lindt JW, Peacock WG, Mitrani-Reiser J, Rosenheim N, Deniz D, Dillard M et al. The Lumberton, North Carolina Flood of 2016: A community resilience focused technical investigation. 2018.

[72] Ren P, Chen X, Sun L, Sun H. Incremental Bayesian matrix/tensor learning for structural monitoring data imputation and response forecasting. *Mechanical Systems and Signal Processing*. 2021;158:107734.

[73] Gelman A, Carlin JB, Stern HS, Rubin DB. *Bayesian data analysis*: Chapman and Hall/CRC; 1995.

[74] Williams CK, Rasmussen CE. *Gaussian processes for machine learning*: MIT press Cambridge, MA; 2006.

[75] Gelfand AE, Diggle P, Guttorp P, Fuentes M. *Handbook of spatial statistics*: CRC press; 2010.

[76] Titsias M. Variational learning of inducing variables in sparse Gaussian processes. *Artificial intelligence and statistics*: PMLR; 2009. p. 567-74.

[77] Hensman J, Fusi N, Lawrence ND. Gaussian processes for big data. *arXiv preprint arXiv:13096835*. 2013.

[78] IN-CORE. Joplin Testbed. 2025.

[79] Kuligowski ED, Lombardo FT, Phan L, Levitan ML, Jorgensen DP. Final report, National Institute of Standards and Technology (NIST) technical investigation of the May 22, 2011, tornado in Joplin, Missouri. 2014.

[80] NOAA. National Oceanic and Atmospheric Administration. Joplin Tornado Images. 2011.

[81] Standohar-Alfano CD, van de Lindt JW. Empirically based probabilistic tornado hazard analysis of the United States using 1973–2011 data. *Natural Hazards Review*. 2015;16:04014013.

[82] WSEC. A recommendation for an Enhanced Fujita Scale. Wind Science and Engineering Center (TTU WiSE), Texas Tech University, Lubbock, Texas. 2006.

[83] FEMA. Hazus Earthquake Model Technical Manual-Hazus 6.1. Federal Emergency Management Agency: Washington, DC, USA. 2024.

[84] Gupta R, Hosfelt R, Sajeev S, Patel N, Goodman B, Doshi J et al. xbd: A dataset for assessing building damage from satellite imagery. *arXiv preprint arXiv:191109296*. 2019.

[85] Braik AM, Salman AM, Li Y. Reliability-based assessment and cost analysis of power distribution systems at risk of Tornado hazard. *ASCE-ASME Journal of Risk and Uncertainty in Engineering Systems, Part A: Civil Engineering*. 2020;6:04020014.

[86] Gardner J, Pleiss G, Weinberger KQ, Bindel D, Wilson AG. Gpytorch: Blackbox matrix-matrix gaussian process inference with gpu acceleration. *Advances in neural information processing systems*. 2018;31.